www.advhealthmat.de

2D Gadolinium Oxide Nanoplates as T_1 Magnetic Resonance Imaging Contrast Agents

Gary Stinnett, Nasim Taheri, Jake Villanova, Arash Bohloul, Xiaoting Guo, Edward P. Esposito, Zhen Xiao, Deanna Stueber, Carolina Avendano, Paolo Decuzzi, Robia G. Pautler, and Vicki L. Colvin*

Millions of people a year receive magnetic resonance imaging (MRI) contrast agents for the diagnosis of conditions as diverse as fatty liver disease and cancer. Gadolinium chelates, which provide preferred T_1 contrast, are the current standard but face an uncertain future due to increasing concerns about their nephrogenic toxicity as well as poor performance in high-field MRI scanners. Gadolinium-containing nanocrystals are interesting alternatives as they bypass the kidneys and can offer the possibility of both intracellular accumulation and active targeting. Nanocrystal contrast performance is notably limited, however, as their organic coatings block water from close interactions with surface Gadoliniums. Here, these steric barriers to water exchange are minimized through shape engineering of plate-like nanocrystals that possess accessible Gadoliniums at their edges. Sulfonated surface polymers promote second-sphere relaxation processes that contribute remarkable contrast even at the highest fields ($r_1 = 32.6 \times 10^{-3}$ M Gd⁻¹ s⁻¹ at 9.4 T). These noncytotoxic materials release no detectable free Gadolinium even under mild acidic conditions. They preferentially accumulate in the liver of mice with a circulation half-life 50% longer than commercial agents. These features allow these T_1 MRI contrast agents to be applied for the first time to the ex vivo detection of nonalcoholic fatty liver disease in mice.

1. Introduction

Roughly sixty million people per year undergo magnetic resonance imaging (MRI). Half of these procedures require Gadolinium-containing contrast agents (CA) to visualize soft tissue, organs, and possible abnormalities associated with disease. [1–3] These clinical contrast agents operate exclusively by

reducing the longitudinal spin magnetization relaxation times (T_1) of protons found mostly in water throughout the body.^[4,5] Other types of MRI contrast, such as that resulting from the reduction of transverse spin relaxation times (T_2) , can be generated from iron oxide nanoparticles. [6] While these materials were approved for use by 2009 by the US FDA, their dark contrast is difficult to interpret as well as concerns about hepatic toxicity from iron overload has led to their commercial failure.[2,3,7-10] As a result molecular T_1 contrast agents remain the gold standard for CA-enhanced MRI. The best agents possess large absolute T_1 relaxivities (r_1) under clinically relevant $(B_0 > 1.4 \text{ T})$ field strengths. Additionally maximum T_1 signal is typically enhanced when there is a match between the longitudinal and transverse relaxation times $(r_2/r_1 \approx 1)$.[3,11,12] When CA meet these conditions the bright features in T_1 -weighted MRI images can lead to definitive diagnoses and treatment monitoring. [1,4,5,10,11]

Eight FDA-approved Gadolinium chelates (GCCA) are available for clinical

use and ongoing research seeks to improve and expand these molecular platforms. [10,13] Gadolinium is an essential component of these materials. With 7 unpaired electrons (S = 7/2), a large magnetic moment (7.94 $\mu_{\rm B}$), and long electron spin relaxation times (10⁻⁹ to 10⁻⁸ s), this atom is ideally suited for promoting the efficient relaxation of water protons. [2,5] However, as the field strength of MRI scanners has increased the performance of these

Dr. G. Stinnett, Prof. R. G. Pautler Department of Molecular Physiology and Biophysics Baylor College of Medicine Houston, TX 77030, USA

Dr. N. Taheri, Dr. A. Bohloul, Dr. C. Avendano Departments of Chemistry and Chemical and Biomolecular Engineering Rice University

Houston, TX 77005, USA

The ORCID identification number(s) for the author(s) of this article can be found under https://doi.org/10.1002/adhm.202001780

DOI: 10.1002/adhm.202001780

J. Villanova, X. Guo, E. P. Esposito, Z. Xiao, D. Stueber, Prof. V. L. Colvin Departments of Chemistry and Engineering

Brown University

Providence, RI 02912, USA

E-mail: vicki_colvin@brown.edu

Prof P Decuzzi

Department of Translational Imaging and Department of Nanomedicine The Methodist Hospital Research Institute

Houston, TX 77030, USA

Prof. P. Decuzzi

Laboratory of Nanotechnology for Precision Medicine Fondazione Istituto Italiano di Tecnologia

Genoa 16163, Italy



conventional contrast agents has fallen as their dominant innersphere relaxation processes are strongly depressed at higher magnetic fields. [11,14–16] One solution is to increase the physical dimensions of the chelates so as to slow their tumbling rates and improve T_1 contrast at higher Larmor frequencies. [1,5,10,17,18] Larger GCCA also provide an avenue for biomolecular conjugation and possible targeting, thereby opening the door to more functional imaging. [1,5,10] Despite these advances, there is growing concern about the nephrogenic toxicity of even these macromolecular contrast agents due to release of Gd^{3+} from their chelators. Several of the commercial GCCA are contraindicated in patients with renal insufficiency due to prolonged circulation times and the European Medicines agency has in 2017 restricted the use of some of the GCCA because of these concerns. [3,10,13,19–22]

Gadolinium-containing nanocrystals offer a promising alternative to molecular Gadolinium complexes for T_1 -enhanced MRI.[23-25] Studies at clinically relevant field strengths report that these materials can possess ionic r_1 (e.g., per [Gd³⁺]) comparable to commercial agents ($r_1 = (3-7) \times 10^{-3} \text{ M Gd}^{-1} \text{ s}^{-1}$) and in some cases even larger r_1 ($\approx 60 \times 10^{-3}$ M Gd⁻¹ s at 1.5 T). [10,15,20,26-39] Johnson et al. formed high-contrast ultrasmall (≈10 nm) NaGdF₄ nanoparticles ($r_1 = 78.2 \text{ mm}^{-1} \text{ s}^{-1}$, $r_2/r_1 = 1.5$, 1.41 T) small enough to undergo clearance through the kidneys. Previous reports demonstrate that the r_1 of pure Gadoliniumcontaining nanocrystals (e.g., Gd₂O₃ or NaGdF₄) is optimized at smaller nanoparticle dimensions presumably because there are proportionally more surface Gd3+ per particle.[20,26,38,40-44] A more relevant metric for nanoparticle CA may be their overall or per-particle contrast. Using this metric, Gd₂O₃ nanoparticles by virtue of the many Gadolinium ions they contain—possess relaxivities thousands of times larger than GCCA. Such high contrast Gadolinium-containing nanocrystals could reduce the effective dosage for CA-enhanced MRI thereby limiting possible toxicity; alternatively, such materials may also enable molecular imaging using MRI to detect small amounts of targeted Gadolinium-containing nanocrystals.[35,39]

Fully realizing the opportunities of these nanocrystal T_1 agents requires a material design that overcomes the apparent contradiction between surface Gd3+ accessibility and the need for particle stability in biological media. Gadolinium must come within 2–3 Å of water in order to affect the most efficient inner-sphere spin relaxation processes.[10,11,14] Such accessibility is not easily achieved as nanocrystal surfaces are necessarily coated with surfactants or polymers that prevent particle aggregation and nonspecific protein adsorption.[41,45–47] One approach is to give up on inner-sphere relaxation processes and amplify the less efficient second-sphere relaxation processes that occur when water associates with ligands bound to the Gadolinium.[16,33,34,38,48-55] As an example, Zheng et al. showed that charged polymer coatings exhibited strong hydrogen bonding with water and resulted in nanoparticles with larger T_1 relaxivities.^[38] 2D nanoparticles could offer a resolution to the problem of surface access: their edges could remain unblocked by coatings thus providing an avenue for the close approach of water while their large faces provide a platform for polymer functionalization. Xiao et al. has explored this strategy with a Gd-doped iron oxide nanoplate but the approach has not been pursued in pure Gadolinium-containing nanomaterials.[35]

Here Gd_2O_3 nanoplates (GONP) by virtue of their unusual shape and highly charged coatings are shown to possess excellent T_1 MRI contrast even at high applied fields. [20,56,57] Inspired by the importance of CA-enhanced MRI in detecting and assessing liver disease, this efforts exploits the role of the liver in nanoparticle clearance and demonstrates how T_1 CA-enhanced MRI from nanoscale materials be used to detect nonalcoholic fatty liver disease (NAFLD).[8,46,58-65] Symptoms of this disease can be aggravated by iron overload, and an iron-free, high r_1 , and liver-specific CA such as the one described here could offer many advantages over the current approaches. [66,67] At clinically relevant field strengths the ionic relaxivities (per [Gd³⁺]) of these nanoplates are almost twenty times larger than the commercial agent, Magnevist (63.0 vs 3.5×10^{-3} M Gd⁻¹ s⁻¹) with a much lower r_2/r_1 (1.17 vs 1.5); per contrast agent the relaxivity (e.g., per particle) is over fifty thousand times larger than commercial contrast agents. The magnetic field (at 1.4, 3, and 9.4 T) and weak size-dependence of their relaxivities suggest that both inner-sphere and secondsphere relaxation mechanisms contribute to their extraordinary performance. These nanoparticles show no appreciable acute in vitro cytotoxicity despite being readily taken into cells where they remain active as T_1 CA. These contrast agents clear the blood and the body approximately twice as fast as molecular agents and distribute through tissues three times slower. They also accumulate more readily in extracellular and intravascular spaces and like many nanoparticles are cleared predominantly hepatically likely via the Kupffer cells of the reticuloendothelial system (RES). The natural biodistribution of these materials suggest opportunities for applying these T_1 CA to liver imaging, and this potential is demonstrated by using nanoscale T_1 CA-enhanced ex vivo MRI to detect early-stage liver disease in an ex vivo mouse model.

2. Results and Discussion

2.1. Synthesis of Gadolinium Oxide Nanoplates

In 2004 Cao was the first to report an approach for forming uniform Gd₂O₃ nanoplates in organic solutions; this route has been fully explored and expanded upon to produce a wide range of rare earth nanoparticles.^[68–75] Specifically, soluble Gadolinium oleate forms at 110 °C from Gadolinium salts, oleyl amine (OLAM), oleic acid (OA), and 1-octadecene. [76] At temperatures greater than 290 °C this precursor decomposes and initiates nucleation and subsequent nanocrystal growth. The dimensions of these materials increase with the ratio of OLAM to OA, as well as time, trends are observed by others who have used a similar chemistry to form other rare-earth and transition metal oxides.[68-75,77] A consistent observation with rare-earth oxide materials, however, is the frequent appearance of plate-like nanocrystals with edge thicknesses on the order of 1 to 2 nm. Some ascribe the asymmetric shape to the particular crystallographic structure of these oxides, while others invoke the influence of soft templating around lamellar micelles formed from aggregated OLAM and OA.[20,72,74] Whatever the mechanism of formation, multiple studies have revealed that these plate-like nanocrystals possess surface coatings bound preferentially to their larger faces. [68,71,74]

Achieving dimensional control over these Gd_2O_3 nanoparticles is important for potential MRI applications as

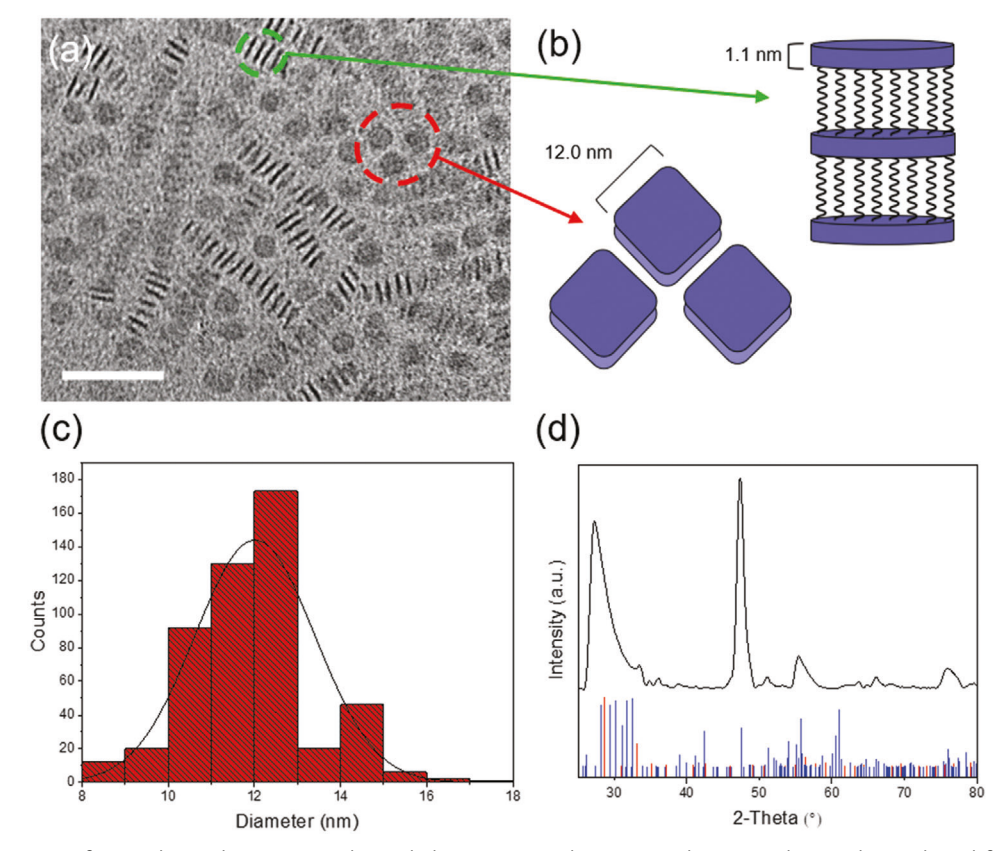


Figure 1. a) TEM image of as-synthesized GONP sample (scale bar = 50 nm). b) Diagram depicting edge-to-edge (red) and face-to-face (orange) alignment of GONP on the TEM grid. c) Size distributions for the diameter of GONP (n = 502). Using a 95% CI and accounting for the resolution limit in the TEM used (0.23 nm), the average diameter of the monodisperse sample is 12.0 \pm 0.36 nm. d) XRD patterns for GONP. The sample diffraction pattern is well matched with the standard JCPDS card for cubic Gd₂O₃ (red) and slightly matched with the standard JCPDS card for monoclinic cubic Gd₂O₃ (blue).

nanocrystalline size is known to affect the relative amount of surface Gadolinium as well as nanoparticle biodistribution, pharmacokinetics, and cellular uptake. [23-25] For the proposed synthesis the overall size of these nanoparticles increases with the ratio of OLAM to OA or with reaction time. This approach yielded a library of Gd₂O₃ nanoparticles with face edges ranging from 2 to 15 nm (Figure S1, Supporting Information). When reaction time was held constant at 18 h, increasing the amount of OA relative to the OLAM resulted in smaller nanoparticles (Figure S1a, Supporting Information). Oleic acid increases the amount of soluble precursor and, therefore, speeds nucleation at the expense of growth. Alternatively, increasing the amount of OLAM apparently promotes nanocrystal growth (Figure S1b, Supporting Information). Since an amino group is a stronger binging ligand for the Gadolinium precursor, its presence results in less rapid decomposition, fewer nucleation events, and consequently larger particles.^[71] Reaction time also increases the dimensions of the nanocrystals, but has the unwanted effect of increasing their size distributions (Figure S1c, Supporting Information). Ostwald ripening can occur at longer reaction times after the precursor Gadolinium is depleted. Because growth can only occur from the dissolution of smaller nanocrystals, the size distributions under these conditions also broaden with time. [78] Because of this, dimensional control in this study was achieved solely through manipulation of the surfactant (OLAM/OA) ratios

The dimensions and morphology of Gd₂O₃ nanoplates (GONP) sample were characterized using transmission electron microscopy (TEM) (Figure 1a). These nanoplates have 12.0 nm faces with thin edges (≈1.1 nm) and relatively uniform dimensional distribution (Figure 1c). Further TEM images show that while face length is varied from 6 to 15 nm (Figure S2a-d, Supporting Information) the GONP edge width remains fixed at ≈1.1 nm, or roughly the length of one unit cell of cubic Gd₂O₃. [69,79] The 2D morphology of these samples is evidenced by edge-to-edge and face-to-face organization on the TEM grid (Figure 1a,b and the inset of Figure S2b in the Supporting Information). X-ray diffraction (XRD) data suggest the presence of cubic ($Ia\bar{3}$) and monoclinic (C2/m) phase bulk Gd_2O_3 (Figure 1d). However, the contributions of monoclinic Gd₂O₃ to the XRD pattern is minor, thus confirming the predominance of cubic phase Gd₂O₃ (bixbyite) in these GONP. Peak broadening is consistent with the small dimensions of the 12.0 nm Gd₂O₃ nanoplates and the peak width for the (440) plane is markedly larger than other reflections which is consistent with the observed 2D morphology of these nanocrystals. The large face of the nanoplate has been reported to vary from squares and rounded squares to quasi-circular polygons, an observation consistent with our own results.[68,70,72,73,77]

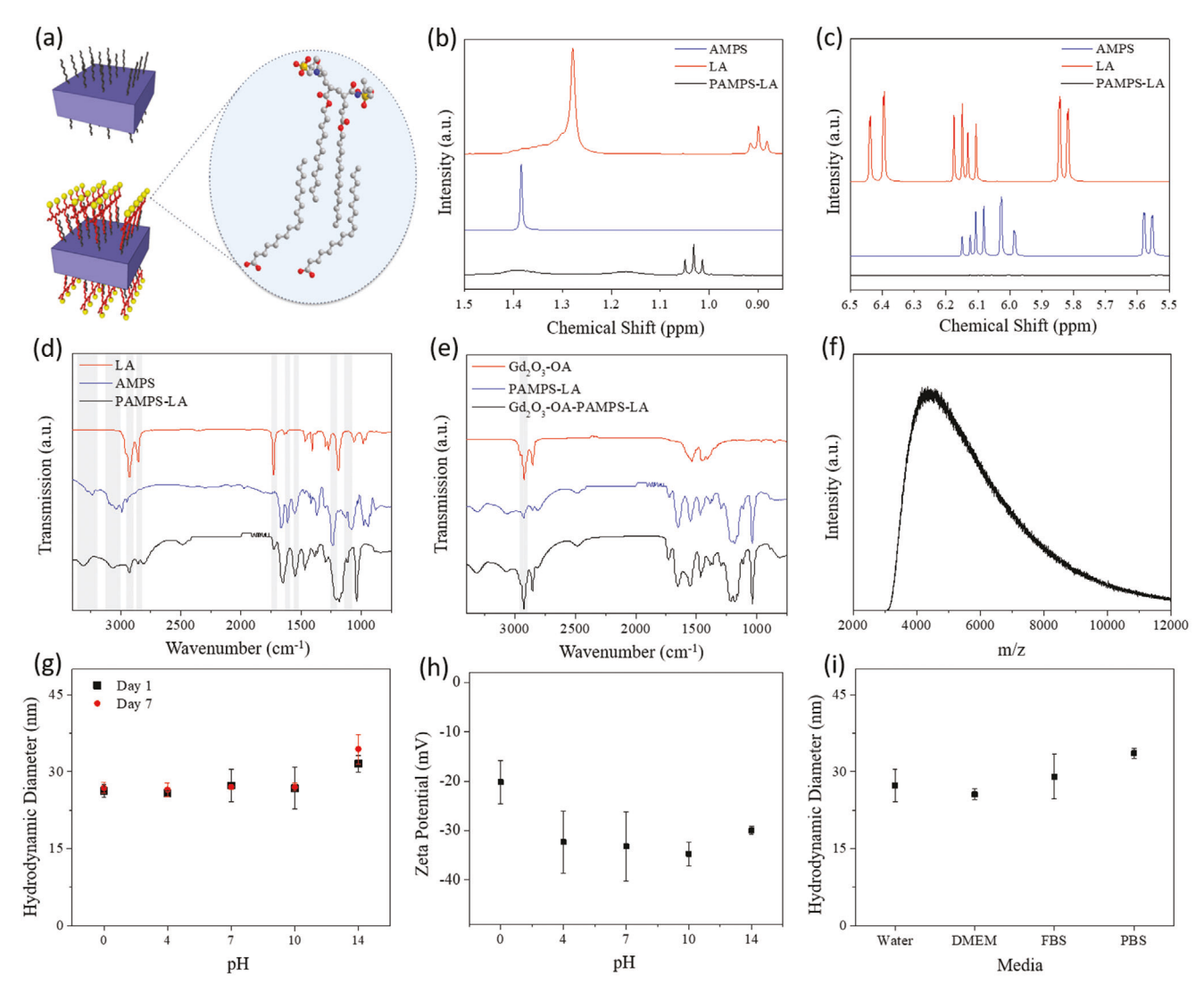


Figure 2. a) Schematic illustration of encapsulation process of GONP using PAMPS-LA amphiphilic copolymer. In this structural model red, gray, blue, and yellow spheres represent oxygen, carbon, nitrogen, and sulfur atoms, respectively. b,c) NMR spectra at different regions for PAMPS-LA and its monomers. d) FT-IR spectra of PAMPS-LA and its monomers and e) GONP before and after PAMPS-LA encapsulation. d,e) Significant peaks highlighted in gray. f) MALDI-TOF mass spectrum of PAMPS-LA polymer with average molecular weight of 4300 Da. DLS data indicating that the g) hydrodynamic diameter and h) zeta potential of GONP-5 remains unchanged over a broad pH range (0–14). i) These nanoplates also demonstrate similar hydrodynamic stability in a variety of biologically relevant dispersion media (water, DMEM, FBS, and PBS). g–i) Reported hydrodynamic diameters and zeta potentials are the average of three independent measurements with the standard deviation represented by error bars.

2.2. Surface Modification of Gadolinium Oxide Nanoplates

To form nonaggregating nanoparticles in aqueous biological media their as-prepared hydrophobic surfaces are typically modified by polymers or surfactants. [47,80,81] These coatings can block water protons from coming within 2–3 Å of surface Gadolinium effectively limiting the most efficient inner-sphere spin relaxation processes. [10,11,14] The 2D geometry of these materials provides a solution to these two opposing materials requirements as illustrated in the scheme (**Figure 2**b) depicting plate-like nanocrystals and the surface-associated polymers. The nanoplates were initially coated with oleic acid (OA); which anchors the hydrophobic end of an amphiphilic copolymer. [80] Due to the formation mechanism of plate-like rare earth oxides, the edges have little

or no OA surface coating.^[20,68,72,74] It is on these narrow edges that surface Gadolinium are located, and are accessible for close, inner-sphere interactions with water protons.^[20,56,57]

Previously several other surface coatings were explored to optimize both colloidal stability and MRI contrast for these nanoplates. [20] Here a sulfonated copolymer, poly (2-acrylamido-2-methylpropane sulfonic acid-lauryl acrylate), or PAMPS-LA, confers excellent colloidal stability while maintaining optimal contrast performance (Figure S3, Supporting Information). Originally developed for use in the harsh environments of oil and gas reservoirs, this class of polymer has not previously been used in nanomedicine. [82,83] Its sulfonic acid functional group ensures excellent colloidal stability over a wide range of conditions and we note that other sulfonated polymers are biocompatible





www.advhealthmat.de

at clinically relevant concentrations.^[82–85] Also, more negatively charged surface coatings enhance the relaxivity of Gadolinium-containing nanocrystals.^[20,38,86] Here we expect that the sulfonic acid groups will structure water around the nanoplates and accelerate second-sphere relaxation processes.^[11,14–16,33,34,38,48–55] Additionally, inner-sphere Gd³⁺—water interactions are facilitated as amphiphilic encapsulation leaves the Gadolinium at the edges uncoated (Figure 2a).

Nuclear magnetic resonance (NMR) and Fourier-transform infrared spectroscopy (FT-IR) were used to characterize PAMPS-LA and encapsulated nanoplates (Figure 2b-e). NMR data confirm the polymerization of AMPS and LA into PAMPS-LA. Vinylic ¹H peaks (5.5–6.5 ppm) in monomers are absent in PAMPS-LA. Also, the methyl group triplet of LA (0.85-1.1 ppm) and singlet of AMPS (1.35-1.45 ppm) are present in PAMPS-LA (Figure 2c). The downfield shift in the methyl triplet from LA to PAMPS-LA is attributed to sulfonate-associated cation deshielding. Broadening of the AMPS methyl singlet in PAMPS-LA is likely due to tumbling rate deceleration. FT-IR data indicate that PAMPS-LA exhibits vibrational modes characteristic of its monomers, but without their C=C stretching mode (1612 cm⁻¹), further confirming AMPS-LA polymerization (Figure 2d). For instance, asymmetric and symmetric S=O stretching (AMPS) at 1238 and 1079 cm⁻¹, AMPS N-H (stretch) and amide (II) at 3236/3038 and 1551 cm⁻¹, and C=O and C-H stretches (LA) at 1729 and 2825/2855 cm^{-1} are all present in PAMPS-LA. Figure 2e shows the IR spectra of as-synthesized nanoplates, PAMPS-LA, and PAMPS-LA coated nanoplates. Spectra of PAMPS-LA-GONP and PAMPS-LA are mostly identical with a stronger presence of CH2 peaks (2924 cm⁻¹) because of the encapsulation of OA. Matrix-assisted laser desorption ionization-time of flight mass spectrometry (MALDI-TOF MS) data indicated a weight average molecular weight of 4300 Da for PAMPS-LA, corresponding to ≈20 monomers (Figure 2f). We found the PAMPS-LA molecular weight to be an important variable to control as larger polymers could cause aggregation and or block edge Gd³⁺-water interactions.

The colloidal stability of encapsulated Gd₂O₃ nanoplates (GONP) in various media was confirmed with dynamic light scattering (DLS) (Figure 2g-i). While hydrodynamic diameter $(D_{\rm H})$ is only a semiquantitative measure of dimension, significant increase in D_H can indicate early stages of aggregation and colloidal instability. [87] The $D_{\rm H}$ for 5 nm GONP (GONP-5) is between 25 and 31 nm, encompassing the Gd₂O₃ core, OA surface layer, PAMPS-LA, and associated electric double layer (Figure 2i; Figure S4, Supporting Information). Due to the acidic nature of the AMPS sulfonate, $D_{\rm H}$ depends only weakly on pH and remains approximately constant over a broad pH range (Figure 2g). However, at conditions below the p K_a of AMPS (1.9), PAMPS-LA becomes slightly more positive (Figure 2h).^[84] Nanoplate average dimensions were also measured in biologically relevant media including Dulbecco's modified Eagle's medium (DMEM), fetal bovine serum (FBS), and phosphate buffer saline (PBS) (Figure 2i; Figure S4, Supporting Information). GONP-5 dimensions remained approximately constant in all these environments.

2.3. Relaxivity Measurements

Water proton relaxation time measurements, both longitudinal (T_1) and transverse (T_2) , as well as the corresponding relaxivities

 $(r_1$ and $r_2)$ and their ratio (r_2/r_1) are an important metric of MRI contrast. Large relaxivities, or fast water proton relaxation rate per Gd³⁺ ion (×10⁻³ м Gd⁻¹ s⁻¹), generally correspond to greater contrast, more resolved MRI data, and lower effective CA dosages. For T_1 CA specifically, the relaxivity ratio (r_2/r_1) should be close to 1 to mitigate confounding effects of M_{xy} on image analysis and consequent reduction in image contrast. [12,88] Commercial, clinically available T_1 contrast agents are molecular Gd³⁺ chelates stable in biological media. For field strengths of 1.5 T, these contrast agents have ionic r_1 between 3 and 7 mm⁻¹ s⁻¹ and relaxivity ratios between 1 and 2.[10,14]

PAMPS-LA encapsulated Gd₂O₃ nanoplates (GONP) have ionic r_1 10–20 times larger than these commercial contrast agents $((60.9-63.0) \times 10^{-3} \text{ M Gd}^{-1} \text{ s}^{-1})$ and r_2/r_1 close to 1 (1.17– 1.29). Ionic relaxivities are weighted necessarily by the amount of Gadolinium that leads to a signal, not the amount of contrast agent; such ionic relaxivities, which report the signal contrast as a function of the molar concentration of Gd3+, are standard metrics for comparing contrast agent design. Figure 3a,b shows the relaxation rates $(1/T_n, n = 1 \text{ or } 2)$ of GONP of varying face length (2, 5, and 12 nm) as a function of Gd3+ concentration. As a benchmark, these data were compared to the response of the commercial contrast agent, Magnevist. These data can be used to determine relaxivity $(r_1 \text{ or } r_2)$ by finding the slope of the linear regression (**Table 1**). The r_1 for the smallest (2 nm, GONP-2) and largest (12 nm, GONP-12) GONP are (61.0 \pm 2.7) $\times\,10^{-3}$ and (63.0 \pm 4.4) $\times\,10^{-3}$ м Gd^{-1} s^{-1} , respectively. These are nearly 20 times larger than the r_1 of Magnevist (3.4 \pm 0.1 mm⁻¹ s⁻¹₁. However, on a per CA basis—which may be the most accurate relaxometric measure of nanoscale CA performance these nanoplates exhibit T_1 relaxivities more than fifty thousand times that of the clinical agent, Magnevist. Also important is the relative ratio of r_2 to r_1 and the r_2/r_1 for these GONP are nearly 1 over a broad range of sizes and magnetic field strengths. Without complex and unconventional pulse sequences, highly active T_2 relaxation can diminish the effect of a T_1 CA as the signal decays due to processes other than those ascribed to T_1 contrast.[12]

The relaxivities $(r_1 \text{ and } r_2)$ of any contrast agent depend on a combination of inner-, second-, and outer-sphere relaxation mechanisms.^[4,5,10] In all cases, protons must come within some distance of magnetically active ion(s) contained in the contrast agent in order to be affected; the underlying mechanism of spin transfer leads to different distance sensitivities.^[4,5,10] Though inner-sphere relaxation mechanisms are usually dominant for molecular contrast agents, the significance of second-sphere processes is also recognized—especially in slower tumbling nanoscale contrast agents. [16,33,34,38,48–55] One characteristic indication of inner-sphere relaxation processes is the strong dependence of r_1 on external magnetic field strength (B_0) . [7,20,26,33,34,38,40,51,81] Caravan et al. showed for molecular complexes that large magnetic fields can quench inner-sphere r_1 yet have little impact on other relaxation processes.^[11] They derived a quantitative relationship for the dependence of r_1 on static B_0 due to inner-sphere relaxation processes.[11,14] According to the model, the maximum in r₁ is achieved once the tumbling rate $(1/\tau_r)$ reaches the proton Larmor frequency (ω_H) ; as the Larmor frequency increases at higher field strengths the relaxivity is expected to fall.[14] For nanoscale and macromolecular CA with

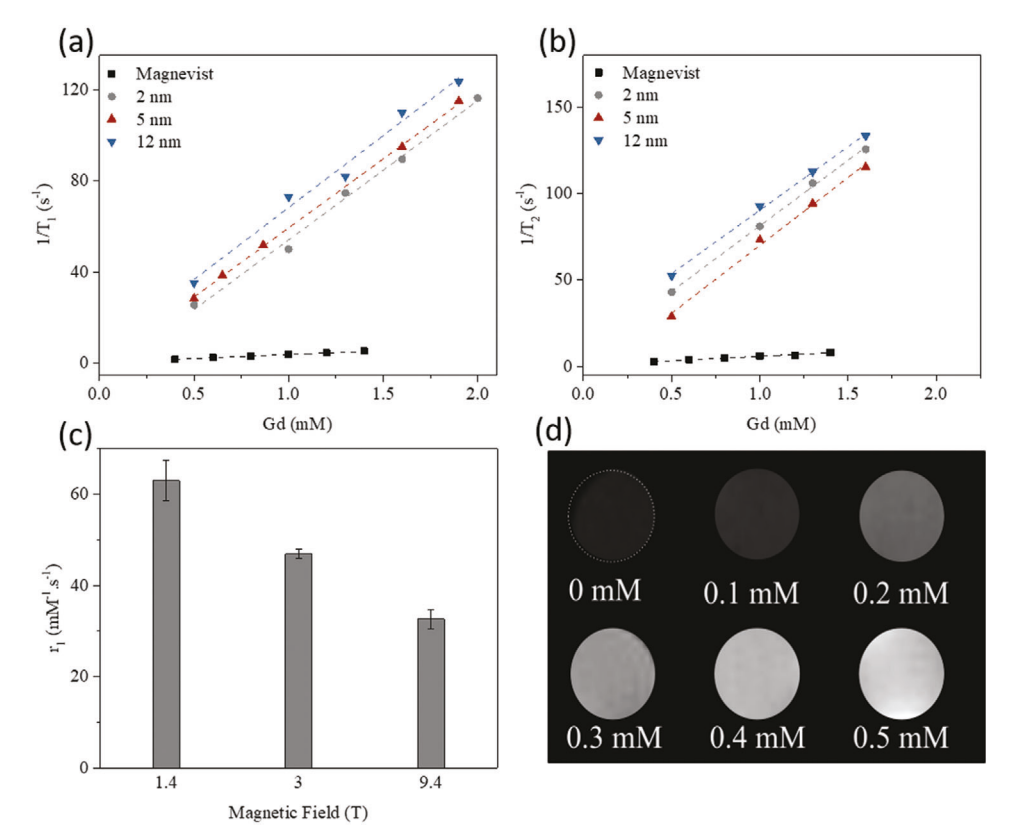


Figure 3. a) Longitudinal and b) transverse relaxation rates as a function of Gadolinium concentration for PAMPS-LA-GONP (2, 5, and 12 nm) compared to Magnevist at 1.4 T. c) R_1 for GONP-12 at 1.4, 3, and 9.4 T are 63.0, 46.9, and 32.6 mm⁻¹ s⁻¹, respectively, thus illustrating its inverse relationship with field strength. d) T_1 -weighted images of GONP (12 nm) at different concentrations of Gadolinium at 9.4 T. a–c) All reported T_1 and T_2 are the average of three independent measurements with the standard deviation represented by error bars.

Table 1. Relaxivity values for PAMPS-LA-GONP and Magnevist in DI water at 1.4 T.

Contrast agent	Core [nm]	$r_1/[Gd^{3+}]$ [mM ⁻¹ s ⁻¹]	r_1/M [(mg mL ⁻¹) ⁻¹ s ⁻¹]	$r_1/\text{NP} [\text{mm}^{-1} \text{ s}^{-1}]$	$r_2/[Gd^{3+}]$ [mm ⁻¹ s ⁻¹]	r_2/M [(mg mL ⁻¹) ⁻¹ s ⁻¹]	r ₂ /NP [mm ⁻¹ s ⁻¹]	r_2/r_1
Magnevist	-	3.5 ± 0.1	-	-	5.1 ± 0.2	-	-	1.5
Gd ₂ O ₃ -PAMPS-LA (GONP-2)	2	61.0 ± 2.7	338	4950	75.9 ± 2.1	419	6160	1.24
Gd ₂ O ₃ -PAMPS-LA (GONP-5)	5	60.9 ± 0.7	336	30 900	78.6 ± 3.6	434	39 800	1.29
Gd ₂ O ₃ -PAMPS-LA (GONP-12)	12	63.0 ± 4.4	348	184 000	$73.5~\pm~2.4$	406	215 000	1.17

slower tumbling rates, the maximum r_1 usually falls between \approx 60 and 100 MHz (\approx 1.4–2.3 T for 1 H). $^{[4,7,33,48]}$

To explore this field dependence over a clinically relevant range, the performance of these materials was measured in different MRI scanners operating at three field strengths, 1.4, 3, and 9.4 T. Figure 3c shows that r_1 decreases as B_0 increases which is consistent with an inner-sphere relaxation mechanism as described by Caravan et al. However, what is notable is that these 2D nanocrystals possess substantial relaxivity at the highest field strengths (32.6×10^{-3} M Gd⁻¹ s⁻¹ at 9.4 T). Commercial molecular contrast agents have T_1 relaxivities of at most $\approx (5-6) \times 10^{-3}$ M Gd⁻¹ s⁻¹ at field strengths above 3 T (Figure S6, Supporting Information). Info.15,33,34] These data illustrate that the nanocrystals studied here also possess substantial second-sphere contri-

butions to their spin relaxation processes which are less sensitive to the applied field.

To further examine the role of second-sphere processes, the performance of the nanocrystals was measured with different surface coatings. Two charged polymer surface coatings (PAMPS-LA and PAA-LA, similar molecular weights) and a neutral polymer coating (PEG) were applied to the same type of Gadolinium-containing nanocrystals (Figure S6 and Table S1, Supporting Information). These data demonstrate that relaxometric performance is severely diminished with a neutral hydrophilic surface coating (PEG) as opposed to highly charged hydrophilic surface coatings with H-bonding capabilities (PAMPS-LA and PAA-LA). Neutral hydrophilic surface coatings are not able to structure water very efficiently, thereby reducing the

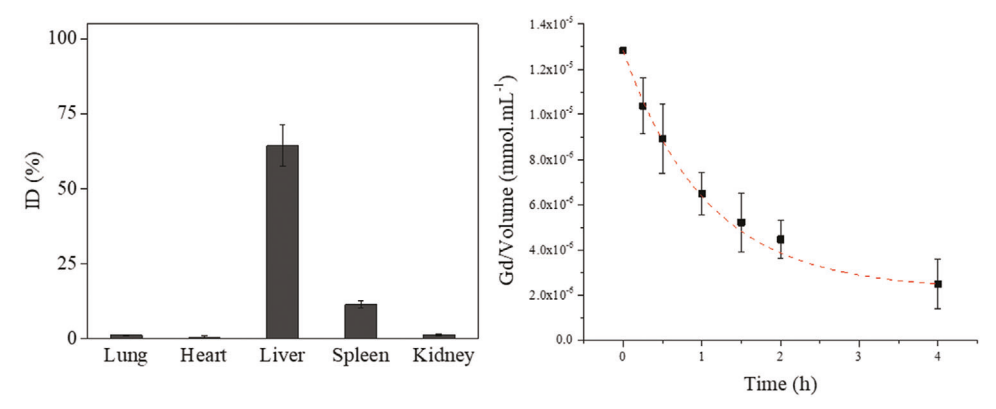


Figure 4. a) Biodistribution profile of GONP-12 measured by percent injection dosage of Gd³⁺ for various organs 24 h after administration. b) Pharmacokinetic profile of GONP-12 measured by Gadolinium per volume blood of mice as a function of time (up to 4 h) after injection in hours. All reported values are the average measurement of six samples (mice) with the standard deviation represented by error bars.

second-sphere contributions to nanoparticle r_1 . [15,16,49,53,55] These results agree with relaxation theory that indicates second-sphere interactions increase with the number of water molecules in that coordination sphere (q'). [15,16] Potential methods for maximizing second-sphere contributions to r_1 would be to increase the grafting density of—or number of charged groups on—the charged, hydrophilic monomer in the encapsulation copolymer.

Notably, while the r_1 of GONP-12 may decrease at higher B_0 , this does not necessarily influence detectability when used for MRI imaging because signal-to-noise ratio (SNR) is known to increase with field strength. [14,89] However, phantom images in Figure 3d show that the optimized nanocrystal contrast agents exhibit significant contrast even at 9.4 T. In conjunction with the direct relationship between field strength and SNR, it can be inferred that these materials would perform exceptionally well at high-field strengths.

Another striking feature of these nanoplates is that their large dimension has little impact on their r_1 (Table 1). The most significant factors affecting the inner-sphere relaxation of a T_1 CA are its tumbling rate, electron spin angular momentum of its magnetically active ion(s) (S), hydration number (q), and the distance between the magnetically active ion(s) and water protons $(r_{\rm H})$. [4,5,10,11,14] Gadolinium(III), with its seven unpaired delectrons, has the largest possible electron spin angular momentum of any metal ion (S = 7/2), which makes it the atom of choice for T_1 CA.^[2,5] Since r_1 is indirectly proportional to the tumbling rate and scales linearly with increasing q, it would be expected that Gadolinium-containing nanocrystals would generally have larger r_1 than molecular contrast agents because of their larger size and low coordination number surface Gadolinium ions.[11,14,15,31,45,47,48,81] Additionally, Gadolinium-containing nanocrystals should allow for cooperative water proton relaxation, an advantage that traditional chelates cannot provide. [31,74] The relatively weak size dependence observed here suggests that vacant edges play a significant role in the relaxation process. Briefly, as nanoplate size increases, the number of surface Gadolinium ions facilitating water proton relaxation per contrast agent volume decreases, a trend that opposes the expected increase in r_1 due to lower tumbling rates. [31,81] The overall magnitude of nanoplate r_1 also indicate the presence of vacant edges because for inner-sphere T_1 relaxation mechanisms, $1/T_1$ decreases with increasing Gd^{3+} —water distance to the power of 6 $(1/T_1 \propto 1/r_{\rm H}^6)$. [4,5,10,11,14] This, along with second-sphere contributions, might explain why, despite being similar in size and composition to other reported Gadolinium-containing nanoparticles, these materials have much larger r_1 at clinically relevant B_0 .

2.4. Pharmacokinetic and Biodistribution Characterization

The pharmacokinetics and biodistribution of MRI contrast agents creates both opportunities and constraints for the imaging of specific organs and diseases. A biodistribution study of GONP-12 24 h after administration confirms the hepatobiliary system as the primary clearance pathway (**Figure 4a**). This is the expected clearance pathway for negatively charged nanomaterials with hydrodynamic diameters of about 25 nm.^[3,23–25,90] In general, the specific hydrodynamic diameter of particles with dimensions between 20 and 100 nm does not significantly impact biodistribution or biological activity. In this size range the surface coating has more influence over clearance times from the blood, and the route of elimination is often observed to be through the reticuloendothelial system (RES).^[3,23–25,46,90]

High accumulation of Gadolinium ions in the liver and spleen provides strong evidence of RES clearance of GONP-12. Phagocytic Kupffer macrophage cells of the liver serve as highly effective hosts for uptake of the negatively surface charged nanocrystals.^[91] This observation was the motivation for the application of GONP-12 to the diagnosis of liver disorders related to macrophage activity such as NAFLD as described later.

After Gadolinium-chelate contrast agents (GCCA) are administered intravenously, they distribute in the blood, the extracellular and intravascular spaces, and are later eliminated from the body through excretory organs. [92] It is well documented that elimination half-life plays an important role in determining the safety of GCCA. In fact, the combination of extended elimination half-life and kinetic stability of GCCA seem to be closely linked to the presence of nephrogenic systemic fibrosis in patients suffering from renal failure and the deposition of Gadolinium in various tissue (brain, bone, skin, etc.) in healthy patients with multiple administrations. [3,10,13,20–22] Though the majority of GCCA are extracellular fluid agents, there are also

ADVANCED HEALTHCARE MATERIALS

Table 2. Plasma kinetics of magnevist and gadolinium oxide nanocrystals.

Contrast agent	Cl _{tot} [mL min ⁻¹ kg ⁻¹]	α _{1/2} [h]	$\beta_{1/2}$ [h]	V _d [L kg ⁻¹]
Magnevist	1.94	0.2	1.6	0.26
GONP-12	1.03	0.6	0.8	0.07

blood-pool agents (Ablavar) and liver-specific agents (MultiHance and Primovist/Eovist). [1,13,21,28,92] Extracellular fluid agents, like Magnevist, distribute in the blood quickly, and in a patient with normal renal function they clear from the blood with an approximate elimination half-life of 1.5 h. [10,24]

It is important to determine how long it takes for GONP-12 to distribute in the body as well as the speed at which they clear from the blood. Figure 4b shows the concentration of Gadolinium in the blood of six healthy mice 4 h postinjection. It is evident from the plasma kinetics that, after an hour, the blood was cleared of half of the initial injection doses of GONP-12. This is compared to the experimental circulation half-life of 1.5 h for commercial Gadolinium chelates.^[10] Moreover, the secondary pharmacokinetic parameters were determined more accurately based on the fit of a two-component biexponential function to the clearance data (Equations (1)–(4) and Table 2).^[92] While more time points would help improve this model, the data collected do allow an estimate of the total clearance rate of the CA based on the blood (Cl_{tot}), the distribution half-life ($\alpha_{1/2}$), the elimination half-life ($\beta_{1/2}$), and the volume of distribution (V_d)

$$C_{\rm P} = A \mathrm{e}^{-at} + B \mathrm{e}^{-bt} \tag{1}$$

$$\alpha_{1/2} = \frac{\ln(2)}{a} \tag{2}$$

$$\beta_{1/2} = \frac{\ln{(2)}}{b} \tag{3}$$

$$Cl_{tot} = V_d \cdot b \tag{4}$$

The distribution half-life for GONP-12 is 0.6 h, which is longer than Magnevist (0.2 h). However, GONP-12 have a shorter elimination half-life (0.8 h) than Magnevist (1.6 h). This means that GONP-12 have a slower distribution rate constant (a in Equations (1) and (2)), and a faster elimination rate constant (b in Equations (1), (3), and (4)). The $0.07 \, L \, kg^{-1}$ volume of distribution for GONP reflects the plasma volume, which suggests their presence in the intravascular space. This stands in contrast to the volume of distribution of Magnevist (0.26 L kg⁻¹), which indicates its presence in the extracellular space. [92] A faster elimination and smaller volume of distribution results in an overall slower total clearance rate of blood for GONP-12 (1.03 mL min⁻¹ kg⁻¹) than for Magnevist (1.94 mL min⁻¹ kg⁻¹). It is well established that as much as 90% of similarly sized, nondegradable nanocrystals are removed from vital organs and excreted over longer periods of time (>7 days), and there is little reason to expect these materials would have significantly different rates of accumulation. [46,93,94] Specifically in the case of several types of Gadolinium-containing nanoparticles at most a few percent of the injected dose remains in the organism after several weeks.^[95–97]

2.5. In Vitro Cellular Uptake, Cytotoxicity, and Gadolinium Release from GONP

The negatively charged surfaces of these nanoplates suggests that they will be readily taken up by phagocytic cells such as macrophages. [91] **Figure 5**a confirms this expectation and shows the amount of Gadolinium taken up by macrophage (Raw 264.7) cells after 24 h of incubation time. The cells exhibit maximal uptake at 50×10^{-6} M of Gd³+. These results are in striking contrast to Magnevist which, after 2 h, only exhibit marginal cellular uptake compared to GONP-12 (Figure S7, Supporting Information). Given their presence inside of cells, there is an opportunity for MRI-based cellular imaging.

Here we investigated whether the high r_1 of $\mathrm{Gd}_2\mathrm{O}_3$ nanoplates (GONP) was maintained intracellularly. Figure 5b shows that relaxation times of cells labeled with GONP dramatically decreased as compared to the unlabeled control cells. In vitro T_1 - and T_2 -weighted images of corresponding cell pellets further confirms the contrast enhancement of labeled cells (Figure S8, Supporting Information). Despite the complex intracellular matrix and the competition that water protons may have with intracellular biomolecules for interaction with the edge Gadolinium, these findings are extremely promising for MR cellular imaging applications such as the visualization of stem cell-based therapies. [98]

Cytotoxicity assays based on 3-(4,5-dimethylthiazol-2-yl)-5-(3-carboxymethoxyphenyl)-2-(4-sulfophenyl)-2H-tetrazolium (MTS) are a convenient, sensitive, and colorimetric method for evaluating cell viability.[98] Using this MTS assay, Raw 264.7 macrophage viability was not significantly affected by incubation with GONP-12 over a wide range of physiologically relevant Gadolinium concentrations (Figure 5c; Figure S9, Supporting Information). GONP retain a viability of nearly 100% at the maximum concentration of 300 \times 10⁻⁶ $\,\mathrm{M}$ (Figure S9d, Supporting Information). These results were confirmed using a live-dead assay which is a common cytotoxicity test used to differentiate viable from nonviable cells based on plasma membrane integrity.[99-101] Fluorescent microscopy of HDF and Raw 264.7 stained cells revealed no cell death even at the highest dose of Gadolinium oxide nanoplates (Figure S9a, Supporting Information). In addition to cell viability, the micrographs show that the spindle shape of HDF cells and the round shape of Raw 264.7 cells were not affected by the addition of different concentrations of surface-coated nanoplates.

A more sensitive cellular assay was applied to measure the effects of nanoparticle exposure on fibroblast function. Commonly referred to as a scratch or wound-healing assay, this test is a straightforward, inexpensive, and well-developed in vitro method for investigating cell migration.^[102] After scratching a monolayer cell culture, the migration of cells to fill the gap over time (wound healing) is observed via an optical microscope.[103] This study can be particularly useful for indirectly investigating the toxic effects of Gd-containing compounds on fibroblasts—a cell type integrally involved in fibrosis and tissue healing in Gd-associated NSF. Optical micrographs of cells incubated with and without nanocrystals were captured at various time intervals as fibroblasts moved to fill in empty space (Figure S9b, Supporting Information). Fibroblasts were remarkably insensitive to GONP and even at the highest nanocrystal concentration (200 \times 10⁻⁶ M) the artificial wound was healed by more than 60% (Figure S9c,

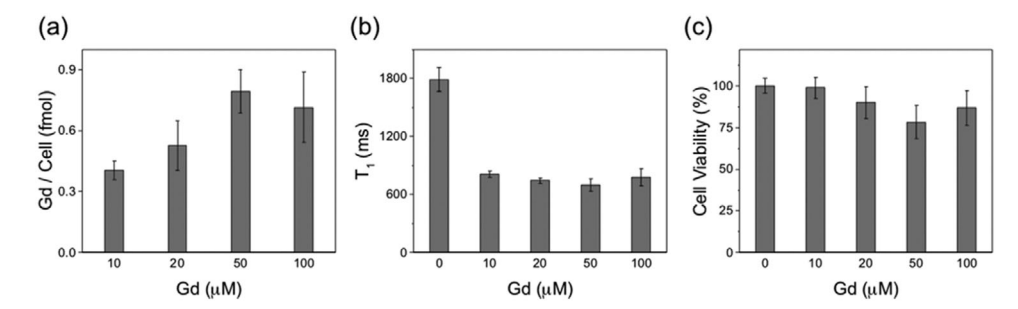


Figure 5. a) Average Gadolinium per cell and b) average T_1 relaxation times of cells (seeding density: 6×10^6 /well) incubated with GONP-12 ((0–100) $\times 10^{-6}$ M Gd³⁺) for 24 h. c) Average viable fraction of cells (seeding density: 2×10^4 /well) incubated with GONP-12 ((0–100) $\times 10^{-6}$ M Gd³⁺) evaluated by MTS assay after 24 h. All reported values are the average of triplicate measurements with standard deviation represented by error bars.

Supporting Information). The results of this experiment may not be representative of an in vivo response, but they do provide a means to screen novel contrast materials based on their more subtle effects on important cellular processes.^[102]

Clinical doses of 0.1 mmol kg $^{-1}$ are typically given for Magnevist, a value approximately equal to the maximum Gadolinium concentration of 300×10^{-6} M used here. [28,92] Given the high r_1 of these nanoplates, and their different possible imaging applications, lower effective dosages would be likely. Further studies of both the acute and chronic toxicity of these materials in vivo are required, but the in vitro cytotoxicity results for nanoplates as compared to Magnevist are promising. [20,31]

To further characterize the safety profile of these nanoparticles, we evaluated their propensity to dissolve (Figure S10, Supporting Information) in a variety of aqueous media. There was no measurable release of Gadolinium from the GONP except under the most acidic (pH = 2) conditions. Samples were placed in dialysis membranes which allowed the passage of free Gadolinium into the dialysate but retained intact nanocrystals.[104,105] After three days of equilibration at a 1:1000 volume ratio, Gadolinium concentrations in both the dialysate and sample were determined by ICP-MS (Figure S10, Supporting Information). No Gadolinium was detected in the dialysate of nanoplate samples except for the most acidic case (pH = 2) and we can conclude that at least 97%of the Gadolinium remained in a nanoparticle form. A longer time study, over several weeks, confirmed that the materials have no measurable ion release even in mildly acidic (pH = 4.3) conditions (Figure S11, Supporting Information). This chemical stability could arise from the particle's organic coatings, or it could reflect the insolubility of bulk Gadolinium oxide in water. Given that a bulk Gadolinium oxide powder did show some, albeit small, release of free Gadolinium in these experiments, we conclude that the surface coatings play some role in protecting these GONP against dissolution.

2.6. Detecting Nonalcoholic Fatty Liver Disease with Gadolinium Oxide Nanoplates

A spectrum liver disorder, nonalcoholic fatty liver disease ranges from relatively benign hepatic steatosis to the necroinflammatory stage of nonalcoholic steatohepatitis, to fibrosis, cirrhosis, and hepatocellular carcinoma. [106] Nonalcoholic fatty liver disease (NAFLD) has emerged as the most common

liver disease, and has been identified as a major public health problem affecting ≈10–40% of the population—depending on sex, geographic location, and diagnostic metric used-in the developed world.[107-109] Disease development and progression is traditionally described as a two-stage process. The first stage is characterized by noninflammatory and nonfibrotic hepatic steatosis—the accumulation of fat in the liver. The second stage, often called nonalcoholic steatohepatitis (NASH), is less well defined but can be characterized by inflammation-induced necrosis, fibrosis, cirrhosis, elevated reactive oxygen species (ROS), hepatocellular carcinoma, liver failure, and increased rate of mortality.^[106–109] Studies show that ≈20% of baseline borderline-NASH NAFLD patients develop NASH and 60% of first stage NAFLD patients develop borderline-NASH or NASH.[109] The cause of this progression to more advanced stages of NAFLD (e.g., NASH) is still under debate, and improved imaging is needed to better understand the disease and its progression.

The traditional method of NAFLD diagnosis and assessment of disease severity is the liver biopsy. However, this method is limited by sampling error and variability, grading inconsistency, and invasiveness. [64,110] As a result, there has been ongoing research into the use of noninvasive imaging to assess the state of the liver using ultrasonography (US), computed tomography (CT), magnetic resonance spectroscopy, and GCCA and ION contrast-based MRI.[8,58-65] Small GCCA such as Magnevist have limited value for liver imaging as they clear through the kidneys; hepatobiliary GCCA, such as Primavist (e.g., gadoxetic acid), can be effective for liver imaging, but their use has been associated with various levels of hepatotoxicity. [29,59,61-63] While the mechanism has not been unequivocally proven, the presence of Gadolinium deposits suggests that the GCCA release toxic, free Gadolinium most likely from acidic lysosomal compartments within the Kupffer cells.[111-113] While nanocrystals are also taken up by Kupffer cells in the liver, the remarkable chemical stability of these materials, even under mildly acidic conditions, should limit the release of free Gadolinium and reduce the likelihood of this particular toxicity mechanism (Figures S9 and S10, Supporting Information).

Nanoparticle-based T_2 CA-enhanced assessment has been used with success in both animal models and humans to assess liver uptake and provide a functional evaluation for NAFLD. [8,58,60,65] As previously mentioned, it is widely accepted that the second stage in NAFLD is characterized by inflammation and the overproduction of reactive oxygen species (ROS). [114] A confounding factor in ROS production is iron

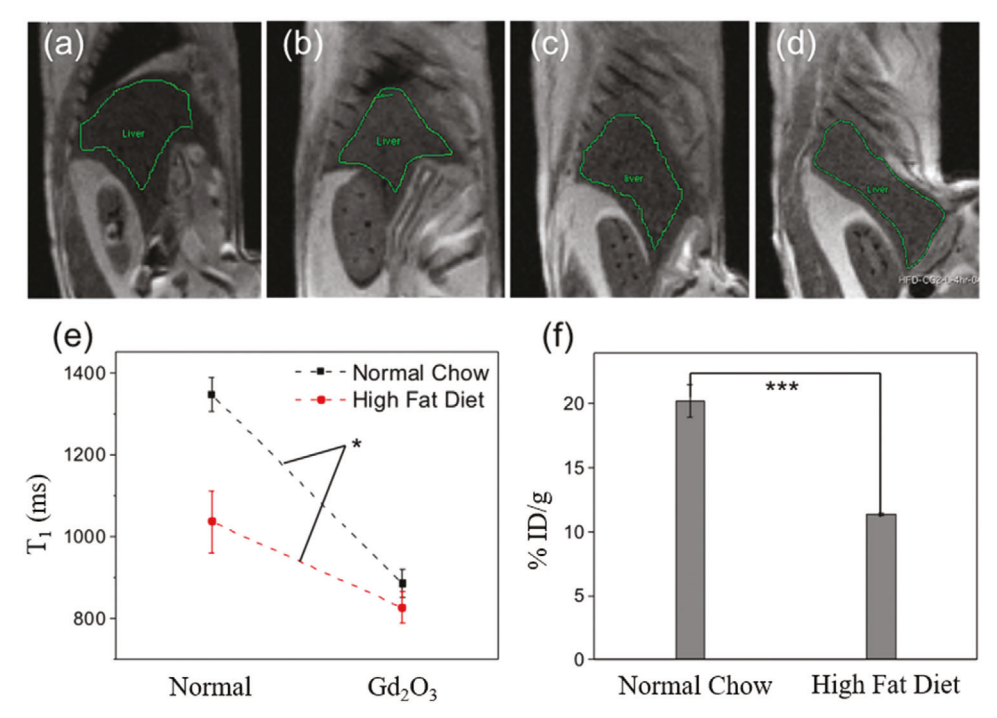


Figure 6. T_1 -weighted images (RAREVTR protocol) of normal chow mice a) without and b) with GONP-12 administration (liver outlined in green). T_1 -weighted images of high fat diet mice c) without and d) with GONP-12 administration (liver outlined in green). All mice with GONP-12 were sacrificed for imaging 4 h after administration. e) Liver T_1 with and without (control) GONP-12. The average liver T_1 of normal chow mice decreased 34.3% compared to a 20.2% decrease for the high fat diet mice. Statistics: Two-way ANOVA. f) Percentage of injected doses of Gadolinium per gram of tissue in normal and fatty liver. The high fat diet mice livers had significantly lower %ID g^{-1} than those of mice fed with normal chow. Statistics: One-way ANOVA. e,f) Reported T_1 and %ID g^{-1} are the average of two samples (mice) with the standard deviation represented by error bars. *p < 0.05, **p < 0.01, and ****p < 0.001.

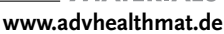
overload, which further increases ROS and other advanced NAFLD symptoms. [66,67] Therefore, an iron-free, high r_1 , and liver-specific CA-based approach to the detection of NAFLD would pose multiple advantages over the current approaches.

To assess liver accumulation of GONP, ex vivo MR imaging was performed 4 h after injection of GONP-12 into live mice (Figure 6a-d). For the purposes of this study, ex vivo MR imaging offers some advantages over in vivo imaging. Ex vivo MR imaging eliminates the need for shorter imaging times and reduces movement artifacts, resulting in better imaging resolution and sensitivity-hence its use elsewhere and in similar applications.[115,116] Both of these advantages are important in an application dependent on quantitatively measuring the differences in the change in contrast enhancement at the same time point postadministration. Liver T_1 were compared between normal and high-fat diet age-matched mice with and without injected GONP-12 (Figure 6e). The effect of nanoplate administration on liver T_1 is assessed using a two-way analysis of variance (ANOVA). The effect of GONP-12 is significantly reduced in the NAFLD, high fat diet, mouse model. Specifically, the decrease in liver T_1 due to GONP-12 administration is significantly smaller in the NAFLD, high fat diet, mouse model than in the age-matched mice fed normal chow. Similar experiments have chosen to use signal intensity or signal-to-noise ratios (SNRs) as a metric for probing uptake. [58,65] However, by averaging curve-fit liver T_1 values from a series of images across multiple rodents, the error included (error bars) reflects both

animal-to-animal variation and the signal-to-noise in the system (Figure 6e,f). The animal-to-animal variation is orders of magnitude larger than that contributed by signal fluctuations and SNR and thus completely defines the reported error. Also, it is thought that calculating relaxation times (T_1) is relatively unaffected by changes in signal and SNR over time, and therefore provides a better quantitative metric of than either. [89] In previous studies, reduced nanoparticle uptake in liver affected by nonalcoholic fatty liver disease is attributed to reduced uptake by hepatic macrophages, or Kupffer cells.^[58] The leading theory to explain reduced uptake involves activation of Kupffer cells by, and increased sensitivity to, lipopolysaccharide endotoxin from gut bacteria due to the accumulation of fatty acids and cholesterol. [117-123] When in this activated state, macrophages demonstrate reduced phagocytosis. [117–123] The average normal chow liver T_1 decrease was 34.3%, compared to a 20.2% average T_1 decrease in the high fat diet mice. After imaging, the liver was dissected and analyzed for Gadolinium content by ICP-MS. The livers of the high fat diet mice had a significantly lower percent injected dose of Gadolinium per gram (%ID g^{-1}) than the normal chow mice (Figure 6f).

In rodent models of nonalcoholic fatty liver disease (NAFLD) using the methionine choline-deficient diet, nanoparticle uptake has been demonstrated to decrease throughout the disease progression, with Kupffer cell populations remaining the same or even increasing.^[60] The measurable decrease in GONP-12 uptake in a mild NAFLD model presented here, as well as the previously reported decrease in phagocytosis throughout disease





ADVANCED HEALTHCARE MATERIALS

progression, demonstrate the opportunity to fully characterize NAFLD mouse models' disease state through a noninvasive T_1 nanoparticle-based MRI.

3. Conclusion

In this study, Gd₂O₃ nanoplates (GONP) were stabilized by an amphiphilic, sulfonated copolymer (PAMPS-LA); these materials demonstrated contrast in T_1 MRI, measured by the relaxivity or r_1 , an order of magnitude larger than commercial T_1 agents. This increase in contrast performance can be attributed is in part due to their plate-like morphology and negatively charged surface coatings which together promote spin relaxation processes. In vitro studies show that, unlike commercial contrast agents, nanoplates are readily taken up by cells where they retain their contrast in MRI. Further development of GONP for clinical applications will require longer term biodistribution studies to quantify clearance from the liver given the growing awareness of the risks of even small accumulations of Gadolinium in the body.[13,21,22,124] Additionally, while the remarkable chemical stability of the Gd₂O₃ nanoplates and their favorable in vitro cytotoxicity profiles suggest a positive biosafety profile, their invivo toxicity remains to be fully characterized. The performance advantages of these high T_1 contrast materials were exploited in the application of GONP to the detection of nonalcoholic fatty liver disease (NAFLD). These imaging results demonstrate the potential of GONP to differentiate and assess NAFLD of different severity in mice. These highly stable Gadolinium-containing nanocrystals have great promise as T_1 contrast agents for the characterization of nonalcoholic fatty liver disease / nonalcoholic steatohepatitis characterization as well as other applications that require targeted T_1 contrast imaging.

4. Experimental Section

Materials: Syntheses requiring inert atmosphere conditions were carried out using high purity Argon gas (>99%) purchased from TechAir. Ethanol (100%) from Koptec USP and acetone (Certified ACS), hexanes (Certified ACS), DMF (Certified ACS), DEE (Certified ACS), methanol (Certified ACS), methanol (HPLC grade), nitric acid (Certified ACS), and water (HPLC grade) from Fisher Chemical were used as received. The following reagents were received from Sigma-Aldrich: 1-octadecene (ODE, 90%), oleylamine (OAm, 70%), oleic acid (OAc, 90%), Gadolinium(III) nitrate hexahydrate (Gd(NO₃)₃·6H₂O, 99.99%), 2,2'-azobis (2-methylpropionitrile) (AIBN, 98%), lauryl acrylate (LA, 90%), 2acrylamido-2-methyl-1-propanesulfonic acid (AMPS, 99%), acrylic acid (AA, anhydrous), poly(ethylene glycol) (PEG, 6 kDa), α -cyano-4hydroxycinnamic acid (MALDI-TOF MS), and Gadolinium standard for ICP (TraceCERT). The following reagents were received from Cambridge Isotope Laboratories, Inc.: chloroform-d (CDCl₃, 99.8%) and deuterium oxide (D₂O, 99.9%). Raw 264.7 cells, DMEM, FBS, PBS, and MTS reagents were obtained from ATCC in Manassas, Virginia. For Gadolinium leaching experiments, bovine calf serum (BCS) was obtained from SAFC (USA sourced) and the DMEM (10x), DPBS (10x), and Gadolinium(III) oxide (≥ 99.9%) were all obtained from Sigma. Unless specified otherwise, all DI water used was purified using a Millipore Milli-Q Water Purification System.

For syntheses requiring photoinitiation, AIBN was further purified as follows: unpurified AIBN in dissolved in methanol at 50 °C, solution filtered into ice bath cooled beaker until recrystallization, and AIBN precipitate vacuum filter dried. All other reagents were used without further purification.

Synthesis and Characterization of Gadolinium Oxide Nanocrystals: In a three-neck flask (50 mL), Gd(NO₃)₃·6H₂O (1.8 g, 4 mmol) was dissolved in oleic acid (1.25-3.75 mL, 4-12 mmol) and 1-octadecene (12.7 mL, 80 mmol). The reaction mixture was heated to 100-110 °C under inert argon atmosphere conditions and medium stir for 5 h to remove low boiling point impurities and generate the clear yellow to light brown Gadolinium oleate precursor. After this period, oleylamine (0-4 mL, 0-12 mmol) was added, followed by raising the temperature to 290 °C for 3-18 h. At this temperature, the Gadolinium oleate complexes decompose, initiating nucleation and nanocrystal growth, generating an opaque brown solution. While still stirring and under argon, solution allowed to cool gradually to room temperature. After cooling, the following purification procedure was done three times: product dissolved in hexanes (5-10 mL), transferred into a centrifuge tube (50 mL) and filled with a solution of ethanol and acetone (1:5 vol%), and centrifuged for 10 min at 10 000 rpm. The final precipitate was resuspended in hexanes (10 mL).

Size, morphology, and composition of nanocrystals were characterized with a JEOL 2100 field emission gun TEM operated at 200 kV with a single tilt holder and a Bruker D8 Discovery 2D X-ray diffractometer operating at 40 kV and 40 mA with a Cu tube (1.5413 Å). Diffraction pattern smoothed using Origin Pro 2016. For TEM, samples were diluted in hexanes until almost colorless and then drop-cast onto Formvar/Carbon coated 400 mesh, copper grids (approximate grid hole size: 42 μm , Ted Pella). For XRD, samples were highly concentrated, drop-cast onto glass slides, and heat-dried.

Synthesis and Characterization of Amphiphilic Polymer (PAMPS-LA): To make PAMPS-LA (Figure S3, Supporting Information), AMPS (0.5175 g, 10 mmol) was dissolved in LA (0.135 mL, 2 mmol) and DMF (3 mL, 155 mmol) in a glass scintillation vial (20 mL). Once completely dissolved, AIBN (3.75 mg, 0.091 mmol) was added as the photoinitiator. The resulting solution was polymerized inside a UV reactor (Luzchem, 253 nm) for 4 h

Polymer synthesis was confirmed using a Thermo Nicolet NEXUS 670 FT-IR with a Mercury Cadmium Telluride (MCT) detector cooled with liquid nitrogen and a Bruker high-field NMR spectrometer (400 MHz) with z-BBFO probe. For NMR, PAMPS-LA (10–20 mg) was mixed with D $_2$ O (700 μ L) and pipetted into an NMR tube for analysis. Monomers (10–20 mg), AMPS and LA, were mixed with D $_2$ O (700 μ L) and CDCl $_3$ (700 μ L) and pipetted into NMR tube for analysis, respectively. NMR spectra were analyzed using TopSpin software.

PAMPS-LA number averaged molecular weight was measured using MALDI-TOF MS. For MS analysis, a 1:1 by volume mixture was made with a solution of PAMPS-LA in ethanol (30–50 mg mL $^{-1}$) and a saturated solution of α -cyano-4-hydroxycinnamic acid (MALDI matrix) in ethanol.

Surface Modification of Gadolinium Oxide Nanocrystals: To achieve dispersion of the nanocrystals in an aqueous phase, PAMPS-LA was used as an encapsulating agent. A 1:1 by volume mixture of a GONP solution in DEE (25 mg mL⁻¹) and a solution of PAMPS-LA in DMF $(80-120 \text{ mg mL}^{-1})$ were added to a glass scintillation vial (20 mL). Both solutions were probe sonicated (Hielscher, UP100H) for 5 min prior to preparing the 1:1 mixture. The mixture was stirred vigorously for 12 h (cap on) to allow encapsulation to occur. After that time, DI water (10 mL) was added to the mixture and stirred vigorously for another 12 h (cap off) to evaporate DMF and DEE and allow the PAMPS-LA encapsulated GONP to transfer into water. After centrifuging the sample for 30 min at 6000 rpm and discarding the precipitate to remove uncoated GONP, the following purification procedure was done three times: separated sample equally between eight ultracentrifuge bottles (26 mL, polycarbonate, Beckman Coulter), filled each bottle with DI water, centrifuged for 1 h at 45 000 rpm using an ultracentrifuge (Beckman Coulter, Optima L-90K), gently extracted supernatant liquid, and resuspended precipitate in DI water. Finally, purified GONP were probe sonicated for 5 min and filtered using 0.2 µm polyethersulfone (PES) membrane filters (Watman, Pauradisk 25 mm syringe filter PES, nonsterile).

Nanocrystal encapsulation was assessed using a Thermo Nicolet NEXUS 670 FT-IR with a Mercury Cadmium Telluride (MCT) detector cooled with liquid nitrogen. Nanocrystal colloidal stability was assessed using hydrodynamic diameter (based on intensity-weighted

ADVANCED HEALTHCARE MATERIALS

measurements; Z-average) and zeta-potential data obtain using a Malvern Zen6300 Zetasizer NanoS equipped with a 633 nm laser.

Relaxivity Measurement and Calculations: The concentration of Gd $^{3+}$ was measured using a Perkin Elmer Nexion 300 inductively coupled optical mass spectrometer (ICP-MS) equipped with an autosampler. The sample preparation started with digesting nanocrystals (100 μ L) in nitric acid (70%, 500 μ L, trace metal basis) on a hotplate at \approx 90 °C for 2 h. Acidified solutions were filtered and diluted to 10 mL with deionized water using a 0.2 μ m PES syringe filter. Calibration curve samples were prepared using dilutions of Gadolinium standard solution (0.5, 1.0, 2.5, 5.0, and 10.0 mg mL $^{-1}$) for ICP (1002 ppm in 2% nitric acid) using nitric acid solution (2%). GONP sample solutions ((0.5–2) \times 10 $^{-3}$ m Gd $^{3+}$) were prepared for relaxometric analysis.

 T_1 and T_2 measurements were carried out on an MR relaxometer (NMR analyzer mq60, Bruker, Billerica, MA) at 1.4 T, and on 3.0 and 9.4 T Bruker Biospec MRI scanners (Bruker BioSpin, Billerica, MA) with varying TR and TE values. The inverse of relaxation time $(1/T_1 \text{ or } 1/T_2, \text{ s}^{-1})$ was plotted as a function of GONP sample Gd^{3+} concentration $(\times 10^{-3} \text{ M})$. A linear regression was made using the GONP sample concentration data points and the ionic relaxivities per Gd^{3+} $(\times 10^{-3} \text{ M Gd}^{-1} \text{ s}^{-1})$ were extracted from its slope. Mass (M) relaxivities $(mL \text{ mg}^{-1} \text{ s}^{-1})$ were calculated from the ionic relaxivities $(r_n, \text{ where } n = 1 \text{ or } 2)$

$$r_n/M\left(\frac{\text{mL}}{\text{mg Gd}_2\text{O}_3*\text{s}}\right) = r_n\left(\frac{\text{L}}{\text{mmol Gd}*\text{s}}\right) \times \frac{2 \text{ mmol Gd}}{1 \text{ mmol Gd}_2\text{O}_3}$$
$$\times \frac{1 \text{ mmol Gd}_2\text{O}_3}{362.49 \text{ mg Gd}_2\text{O}_3} \times \frac{1000 \text{ mL}}{1 \text{L}}$$
(5)

Assuming a circular GONP of dimensions 12.0 \times 1.1 nm, the per CA relaxivity ($\times 10^{-3}$ M CA⁻¹ s⁻¹) was calculated as follows

$$\begin{split} M_{GONP} &= \left(\pi \times \left(\frac{1.2 \times 10 \text{ cm}}{2}\right)^2 \times 1.1 \times 10^{-7} \text{ cm}\right) \times \frac{7070 \text{ mg Gd}_2 \text{O}_3}{1 \text{ mL}} \\ &\times \frac{1 \text{ g}}{1000 \text{ mg}} = \frac{8.80 \times 10^{-19} \text{ g Gd}_2 \text{O}_3}{1 \text{ GONP}} \end{split} \tag{6} \\ r_1/\text{NP}\left(\frac{\text{L}}{\text{mmol GONP} * \text{s}}\right) &= r1 \left(\frac{\text{L}}{\text{mmol Gd} * \text{s}}\right) \times \frac{2 \text{ mmol Gd}}{1 \text{ mmol Gd}_2 \text{O}_3} \\ &\times \frac{1 \text{ mmol Gd}_2 \text{O}_3}{362.49 \text{ mg Gd}_2 \text{O}_3} \times \frac{1000 \text{ mg Gd}_2 \text{O}_3}{1 \text{ g Gd}_2 \text{O}_3} \times \frac{6.022 \times 10^{23} \text{ GONP}}{1 \text{ mol GONP}} \\ &\times \frac{1 \text{ mol GONP}}{1000 \text{ mmol GONP}} \tag{7} \end{split}$$

Biodistribution and Pharmacokinetics: All animal work for this study was performed in Association for Assessment and Accreditation of Laboratory Animal Care (AAALAC) accredited facilities, and the Institutional Animal Care and Use Committee approved all procedures (T-23411). To accomplish biodistribution studies, six C57BL/6-J immune-competent mice (6 months old) were injected with Gadolinium oxide nanocrystals (100 μL of 2.5×10^{-3} M) in PBS via tail vein. Mice were sacrificed by cervical dislocation and tissue was obtained and weighed for measurement by ICP-MS (Perkin Elmer Nexion 300) at 24 h postinjection. Organ weights are as follows: lungs (0.5285 g), heart (0.598 g), liver (1.5360 g), spleen (0.2151 g), and kidneys (0.3578 g). For pharmacokinetic studies, blood (20 μL) was drawn at time intervals up to 4 h postinjection and stored in glass vials for ICP-MS analysis.

Cell Labeling: Cell labeling was conducted in preparation for internalization, MRI, and cell viability studies. First, macrophage (Raw 264.7) cells were cultured over a certain amount of time in DMEM with penicillin (1%) and FBS (10%). For the purposes of MR imaging, cell pellets of 6 million cells or larger are required; therefore, cells were separated into aliquots of at least 6×10^6 cells and seeded into 6-well cell culture plates. Cell labeling was carried out by adding Gadolinium oxide nanocrystals or Magnevist $(0-100\times10^{-6}~\text{M})$ for 24 or 2 h at 37 °C and CO $_2$ (5%). After Trypsiniza-

tion, cells were washed 2 times in PBS and then pelleted a third time in PCR tubes for imaging or ICP-MS experiments.

Cell Viability Assay: An MTS toxicity assay was performed in a 96-well plate for Raw 264.7 macrophages, and each dataset was measured in triplicate. When preparing the assay after detachment from the original culture flask, cells were plated in the first three rows of a 96-well plate (seeding density: $2\times10^4/\text{well}$, $100~\mu\text{L}$). The fourth 96 row was filled with $100~\mu\text{L}$ media without cells to act as the blank. In rows 1–3, $20~\mu\text{L}$ of nanocrystals with various concentrations was added from columns 3–11 (this step was repeated in exactly the same manner for the 2nd and 3rd rows). Instead of nanocrystals, the 1st column was filled with $20~\mu\text{L}$ of PBS (negative control). The last column (12th) was filled with $20~\mu\text{L}$ of ethanol (positive control) to produce dead cells. Rows 5–9 were filled in the same way, but with different concentrations of nanocrystals.

The prepared 96-well plates were placed in the incubator for 24 h. After the incubation period, the solutions were removed from all wells using glass pipettes attached to the aspiration tube and fresh prewarmed media (100 μ L), and an MTS reagent (20 μ L) was subsequently added to all wells. After another 1 h incubation period, absorbance of each well at 490 nm was measured using a microplate reader (TECAN Infinite M1000).

To calculate cell viability, first the average absorbance of blank wells was subtracted from the negative control wells, nanocrystal-containing wells, and positive control wells to remove the absorbance of media or nanocrystals. Then the average absorbance of all wells (except the blank wells) was divided by the average absorbance of the negative control. In this study, all negative control cells were considered viable cells where cell viability is the percentage of the resulting value.

Live—Dead Assay: For the live—dead cytotoxicity assay, cell media were aspirated after HDF and Raw 264.7 cells were incubated with nanocrystals for the desired period of time. Cells were then washed three times with PBS to remove any media residue. The working solution of dyes was prepared fresh by diluting the assay dyes in PBS with the final concentration of 2×10^{-6} M of calcein-AM dye and 4×10^{-6} M of ethidium homodimer-1 (EthD-1). To achieve these concentrations, a 20 µL of 2×10^{-3} M EthD-1 stock solution was first added to 10 mL of PBS and vortexed to ensure complete mixing (with a final concentration of 4×10^{-6} M). Second, 5 µL of 4×10^{-3} M calcein-AM was added to the mixture to achieve the final concentration of 2×10^{-6} M of calcein-AM. These working solutions were then added directly to the cells (1 mL in each well on the 6-well plate). Cells were incubated for 30–45 min at room temperature before observing them under the fluorescence microscope (EVOS fluorescence microscope).

Wound-Healing Assay: For the wound-healing assay, HDF cells were seeded and cultured in the marked 6-well plate until they became nearly confluent (80–90%). Media was aspirated, and then the surface of the cells was scratched using a 100 μL pipette tip moving perpendicular to the line marked at the back of the plate. Next, the cells were washed gently with PBS to remove the dead scratched cells, and prewarmed media containing different concentrations of nanocrystals were added. After certain time intervals (0, 2, 6, 15, 24, and 48 h), wounds were inspected microscopically (4× and 10× magnifications) with an orientation at the cross point of the wound and the marked line.

Mouse Model for Nonalcoholic Fatty Liver Disease Application: A mouse model was used to study the application of the nanocrystals in MR imaging to assess for nonalcoholic fatty liver disease. Wild-type immune-competent mice on background C57B6/J were fed a 60% kcal fat diet for seven months (D12492, Research Diets, New Brunswick, NJ, USA). This mouse model is beginning to exhibit elevated alanine aminotransferase and aspartate aminotransferase levels, which is often used as an indicator of onset NAFLD.

For this experiment, mice were injected with Gadolinium oxide nanocrystals (11 nmol g $^{-1}$, GONP-12) via tail vein from a stock solution containing Gd $^{3+}$ in DI water (7.6 \times 10 $^{-3}$ M). Controls were left uninjected. Four hours after administration, mice were sacrificed by cervical dislocation and immediately imaged in the MRI. Mice were maintained at 37 °C by rectal temperature probe and heated air circulation.

Ex Vivo MR Imaging: Ex vivo MR imaging was performed on the mice after they were sacrificed. Images were acquired on a 9.4 T Bruker





www.advhealthmat.de

AvanceBiospec Spectrometer, 21 cm bore horizontal scanner with a 72 mm volume resonator (Bruker BioSpin, Billerica, MA) with Paravision 5.1 software (Bruker BioSpin, Billerica, MA). Mice were imaged using a Rapid Acquisition with Refocused Echoes protocol with Variable Acquisition repetition time (RAREVTR) TR = 30.984–15 000 ms (five images), TE = 6.57 ms, RF = 4, FOV = 3×3 cm, matrix size = 128×128 , 11 m, 48 s, and 399 ms. Beforehand, acquisition on a FLASH tripilot was run for placement. Liver T_1 was measured in the sagittal plane, and slices were aligned with the right kidney to ensure consistent measurement. Liver was masked out and analyzed for T_1 time in Paravision 5.1. T_1 calculations were done using the built-in tools in Paravision 5.1.

Gadolinium Leaching: Dialysis experiments coupled with ICP-AES were used to determine the amount of Gd³⁺ leaching from Gd-containing samples (GONP, bulk Gd₂O₃, or Gd(NO₃)₃) dispersed in a variety of biologically relevant media (water, pH 4-4.5, pH 2, PBS, DPBS, or BCS) over time (3, 7, 14, and 20 days). Stock sample Gd3+ concentrations were approximately (3–4) $\times~10^{-3}$ m for GONP, 50×10^{-3} m for bulk $Gd_2O_3,$ and 5×10^{-3} M for Gd(NO₃)₃. Spectra/Por 6 dialysis membranes (prewetted RC tubing, 1 kDa MWCO) were used in all dialysis experiments. A Thermo Scientific iCAP 7400 DUO inductively coupled plasma atomic emission spectrometer was used to measure Gd3+ concentrations of samples, tubing, and dialysate. Samples were digested with tubing in a Milestone Ultrawave SRC microwave digestion system in preparation for ICP analysis. Calibration curve standards were prepared using 0.044, 0.082, 0.248, 0.490, 0.992, 2.493, 5.012, 9.267, and 49.408 ppm dilutions of a Gadolinium standard solution for ICP (1002 ppm Gd³⁺ in 2% nitric acid) using 2% nitric acid solution. The following experiments always had total mass recoveries of more than 85%, except in the case of Nano Gd₂O₃ in BCS.

For 3 day dialysis experiments, ≈1 mL of sample (GONP, bulk Gd₂O₃, or Gd(NO₃)₂) was pipetted into a 3-4 in. section of dialysis tubing, sealed with clips, and placed in a beaker of medium (water, pH 4-4.5, pH 2, PBS, DMEM, or BCS) on continuous stir for three days. Samples were often diluted (99/100 or 9/10) to achieve the same media concentration as the dialysate without reducing the Gd³⁺ concentration too much. Also, in the case of the bulk powder homogeneous solution could not be prepared, and micrograms of material weighed on an analytical balance were introduced in the media with vortexing. The concentration of these bulk powders was as a result ten times larger than that of the nanoparticles and Gadolinium salt. Experiments using BCS required a 1/10 dilution of samples to maintain a BCS concentration as close to 100% as possible (90%). For water, pH 4-4.5, pH 2, and PBS, the volume ratio of sample to dialysate was 1:1000. For BCS experiments the volume ratio of sample to dialysate was 1:100. After three days, dialysate and samples (with tubing) were collected, digested, and prepared for ICP analysis. Experiments performed in triplicate unless noted otherwise.

For time-dependent dialysis experiments, ≈ 0.9 mL of sample (GONP, bulk Gd_2O_3 , and $Gd(NO_3)_3$) was pipetted into a 3–4 in. section of dialysis tubing, sealed with clips, and placed in a beaker of medium (water, pH 4–4.5, pH 2, or PBS) for 20 days. Beakers were stirred twice daily, and 10 mL of dialysate was collected at 3, 7, 14, and 20 days for ICP analysis. Some samples were diluted (99/100 or 9/10) to achieve the same media concentration as the dialysate without reducing the Gd^{3+} concentration too much. After 20 days, samples (with tubing) were collected, digested, and prepared for ICP analysis.

Statistical Analysis: Electron microscopy was used for dimensional measurement (Figure 1; Figures S1 and S2, Supporting Information). TEM images of nanoplate samples were saved as TIF and Gatan DigitalMicrograph Image Document 3 files. For each sample, the dimensions (face length and width) of a minimum of 200 particles (Figures S1 and S2, Supporting Information) or 500 particles (Figure 1) were manually measured using the image processing software Image). The average (reported throughout and in Figure 1, Figures S1 and S2 in the Supporting Information, and Table 1), standard deviation (reported throughout and as error bars in Figures S1 and S2 in the Supporting Information), and the margin of error based on a 95% C1 and resolution limit of 0.23 nm (Figure 1) of the nanoplate dimensions are reported.

Relaxivity was found as described previously in the Experimental Section. The inverse of longitudinal and transverse relaxation times $(1/T_1)$ or

 $1/T_2$, s^{-1}) were plotted as a function of GONP sample Gd^{3+} concentration ($\times 10^{-3}$ M). A linear regression of each data set was made and ionic relaxivities per Gd^{3+} ($\times 10^{-3}$ M Gd^{-1} s⁻¹) were extracted from its slope. The reported average relaxivity (or individual T_1) and standard deviation (reported with mean throughout and as error bars) were calculated from the results of three independent experiments (Figures 3, 5, and 6 and Table 1; Figures S1 and S5–S7, Supporting Information). Quantification of Gd^{3+} content in solutions, organs and nanoparticles using ICP-MS were done using calibration curves as discussed previously in the Experimental Section. All measurements were performed in triplicate except for the biodistribution, pharmacokinetic, and ex vivo T_1 -weighted imaging experiments. The sample sizes for the biodistribution and pharmacokinetic experiments were six (Figure 4). The sample sizes for the ex vivo T_1 -weighted images were two (Figure 6). Gadolinium concentrations and % ID are reported as the average with the standard deviation as error bars (Figures 4 and 5; Figures 57, Supporting Information).

DLS measurements were performed in triplicate. Hydrodynamic size (based on intensity-weighted measurements; *Z*-average) and zeta potential are reported as the average with the standard deviation as error bars (Figure 2).

Student's *t*-test was used to analyze the significance of differences in liver T_1 and Gd^{3+} content for mice with fatty and normal diets (Figure 6). The significance of difference becomes greater with decreasing *p*-value (significant difference, p < 0.05; very significant difference, p < 0.01; extremely significant difference p < 0.001)

All statistical analyses performed in Microsoft Office $\ensuremath{\mathsf{Excel}}$ and or Origin Pro.

Supporting Information

Supporting Information is available from the Wiley Online Library or from the author.

Acknowledgements

G.S., N.T., and J.V. contributed equally to this work. The authors acknowledge the support given by the Baylor College of Medicine Small Animal MRI, Texas Children Hospital Small Animal Imaging Facilities, Houston Methodist Research Institute, and Rice University Shared Equipment Authority. This work was supported by a training fellowship from the Keck Center Nanobiology Training Program of the Gulf Coast Consortia (NIH Grant No. T32 EB009379-04) and the Belfer Foundation, and the National Institutes of Health (R01EY030569).

Conflict of Interest

The authors declare no conflict of interest.

Data Availability Statement

Research data are not shared.

Keywords

gadolinium oxide nanocrystals, magnetic resonance imaging, nanoplates, nonalcoholic fatty liver disease, T_1 contrast agents

Received: October 12, 2020 Revised: February 18, 2021 Published online:

[1] Y. Cao, L. J. Xu, Y. Kuang, D. S. Xiong, R. J. Pei, J. Mater. Chem. B 2017, 5, 3431.



www.advhealthmat.de

HEALTHCARE

- [2] L. Faucher, M. Tremblay, J. Lagueux, Y. Gossuin, M. A. Fortin, ACS Appl. Mater. Interfaces 2012, 4, 4506.
- [3] H. Wei, O. T. Bruns, M. G. Kaul, E. C. Hansen, M. Barch, A. Wisniowska, O. Chen, Y. Chen, N. Li, S. Okada, J. M. Cordero, M. Heine, C. T. Farrar, D. M. Montana, G. Adam, H. Ittrich, A. Jasanoff, P. Nielsen, M. G. Bawendi, Proc. Natl. Acad. Sci. USA 2017, 114, 2325.
- [4] R. B. Lauffer, Chem. Rev. 1987, 87, 901.
- [5] D. L. Ni, W. B. Bu, E. B. Ehlerding, W. B. Cai, J. L. Shi, Chem. Soc. Rev. 2017, 46, 7438.
- [6] Y. Li, D. Xu, H.-N. Chan, C.-Y. Poon, S.-L. Ho, H.-W. Li, M. S. Wong, Small 2018, 14, 1800901.
- [7] L. Faucher, A. A. Guay-Begin, J. Lagueux, M. F. Cote, E. Petitclerc, M. A. Fortin, Contrast Media Mol. Imaging 2011, 6, 209.
- [8] Y. X. J. Wang, J. M. Idee, Quant. Imaging Med. Surg. 2017, 7, 88.
- [9] M. Jeon, M. V. Halbert, Z. R. Stephen, M. Zhang, Adv. Mater. 2020, 1906539.
- [10] J. Wahsner, E. M. Gale, A. Rodriguez-Rodriguez, P. Caravan, Chem. Rev. 2019, 119, 957.
- [11] P. Caravan, J. J. Ellison, T. J. McMurry, R. B. Lauffer, Chem. Rev. 1999, 99, 2293.
- [12] G. E. Hagberg, K. Scheffler, Contrast Media Mol. Imaging 2013, 8,
- [13] T. J. Fraum, D. R. Ludwig, M. R. Bashir, K. J. Fowler, J. Magn. Reson. Imaging 2017, 46, 338.
- [14] P. Caravan, Chem. Soc. Rev. 2006, 35, 512.
- [15] P. Caravan, C. T. Farrar, L. Frullano, R. Uppal, Contrast Media Mol. Imaging 2009, 4, 89.
- [16] V. Jacques, S. Dumas, W. C. Sun, J. S. Troughton, M. T. Greenfield, P. Caravan, *Invest. Radiol.* 2010, 45, 613.
- [17] Z. Wei, Z. Jiang, C. Pan, J. Xia, K. Xu, T. Xue, B. Yuan, O. U. Akakuru, C. Zhu, G. Zhang, Z. Mao, X. Qiu, A. Wu, Z. Shen, Small 2020, 16, 1906870.
- [18] H. Zhang, Y. Wu, J. Wang, Z. Tang, Y. Ren, D. Ni, H. Gao, R. Song, T. Jin, Q. Li, W. Bu, Z. Yao, Small 2018, 14, 1702951.
- [19] Reactions Weekly 2017, 1663, 2.
- [20] M. J. Cho, R. Sethi, J. S. A. Narayanan, S. S. Lee, D. N. Benoit, N. Taheri, P. Decuzzi, V. L. Colvin, Nanoscale 2014, 6, 13637.
- [21] J. W. Choi, W. J. Moon, Korean J. Radiol. 2019, 20, 134.
- [22] L. Fur, M. P. Caravan, Metallomics 2019, 11, 240.
- [23] P. Decuzzi, B. Godin, T. Tanaka, S. Y. Lee, C. Chiappini, X. Liu, M. Ferrari, J. Controlled Release 2010, 141, 320.
- [24] F. Alexis, E. Pridgen, L. K. Molnar, O. C. Farokhzad, Mol. Pharmaceutics 2008. 5. 505.
- [25] C. B. He, Y. P. Hu, L. C. Yin, C. Tang, C. H. Yin, Biomaterials 2010, 31, 3657.
- [26] N. J. J. Johnson, S. He, V. A. N. Hun, A. Almutairi, ACS Nano 2016, 10, 8299.
- [27] Y. Kuang, Y. Cao, M. Liu, G. Y. Zu, Y. J. Zhang, Y. Zhang, R. J. Pei, ACS Appl. Mater. Interfaces 2018, 10, 26099.
- [28] J. Lohrke, T. Frenzel, J. Endrikat, F. C. Alves, T. M. Grist, M. Law, J. M. Lee, T. Leiner, K. C. Li, K. Nikolaou, M. R. Prince, H. H. Schild, J. C. Weinreb, K. Yoshikawa, H. Pietsch, Adv. Ther. 2016, 33, 1.
- [29] R. Meenambal, P. Poojar, S. Geethanath, S. Kannan, J. Biomed. Mater. Res., Part B 2017, 105, 2545.
- [30] D. L. Ni, J. W. Zhang, J. Wang, P. Hu, Y. Y. Jin, Z. M. Tang, Z. W. Yao, W. B. Bu, J. L. Shi, ACS Nano 2017, 11, 4256.
- [31] J. Y. Park, M. J. Baek, E. S. Choi, S. Woo, J. H. Kim, T. J. Kim, J. C. Jung, K. S. Chae, Y. Chang, G. H. Lee, ACS Nano 2009, 3, 3663.
- [32] P. Sanchez, E. Valero, N. Galvez, J. M. Dominguez-Vera, M. Marinone, G. Poletti, M. Corti, A. Lascialfari, *Dalton Trans.* 2009, 800.
- [33] Z. Y. Shen, W. P. Fan, Z. Yang, Y. J. Liu, V. I. Bregadze, S. K. Mandal, B. C. Yung, L. S. Lin, T. Liu, W. Tang, L. L. Shan, Y. Liu, S. J. Zhu, S. Wang, W. J. Yang, L. H. Bryant, D. T. Nguyen, A. G. Wu, X. Y. Chen, Small 2019, 15, 9.

- [34] Z. Y. Shen, T. Liu, Z. Yang, Z. J. Zhou, W. Tang, W. P. Fan, Y. J. Liu, J. Mu, L. Li, V. I. Bregadze, S. K. Mandal, A. A. Druzina, Z. N. Wei, X. Z. Qiu, A. G. Wu, X. Y. Chen, *Biomaterials* 2020, 235, 119783.
- [35] N. Xiao, W. Gu, H. Wang, Y. L. Deng, X. Shi, L. Ye, J. Colloid Interface Sci. 2014, 417, 159.
- [36] L. Y. Zeng, D. Wu, R. F. Zou, T. X. Chen, J. C. Zhang, A. G. Wu, Curr. Med. Chem. 2018, 25, 2970.
- [37] Y. Zeng, L. Q. Wang, Z. J. Zhou, X. Y. Wang, Y. Zhang, J. Q. Wang, P. Mi, G. Liu, L. M. Zhou, Biomater. Sci. 2017, 5, 50.
- [38] X. Y. Z. K. Zheng, J. Tang, X. Y. Wang, L. D. Li, N. X. Chen, Y. J. Wang, S. Shi, X. Zhang, S. Malaisamy, L. D. Sun, X. Wang, C. Chen, C. H. yan, ACS Nano 2017, 11, 3640.
- [39] Z. J. Zhou, D. T. Huang, J. F. Bao, Q. L. Chen, G. Liu, Z. Chen, X. Y. Chen, J. H. Gao, Adv. Mater. 2012, 24, 6223.
- [40] S. He, N. J. J. Johnson, V. A. N. Huu, E. Cory, Y. R. Huang, R. L. Sah, J. V. Jokerst, A. Almutairi, *Nano Lett.* **2017**, *17*, 4873.
- [41] N. J. Johnson, W. Oakden, G. J. Stanisz, R. S. Prosser, F. van Veggel, Chem. Mater. 2011, 23, 3714.
- [42] F. Y. Li, Z. Y. Liang, J. N. Liu, J. H. Sun, X. Hu, M. Zhao, J. X. Liu, R. L. Bai, D. Kim, X. L. Sun, T. Hyeon, D. S. Ling, *Nano Lett.* **2019**, *19*, 4213.
- [43] H. Y. Lin, K. Liu, J. H. Gao, Eur. J. Inorg. Chem. 2019, 2019, 3801.
- [44] Z. J. Zhou, L. J. Yang, J. H. Gao, X. Y. Chen, Adv. Mater. 2019, 31, 32.
- [45] M. A. Fortin, R. M. Petoral, F. Soderlind, A. Klasson, M. Engstrom, T. Veres, P. O. Kall, K. Uvdal, *Nanotechnology* 2007, 18, 395501.
- [46] G. Yang, S. Z. F. Phua, A. K. Bindra, Y. Zhao, Adv. Mater. 2019, 31, 1805730.
- [47] M. Ahrén, L. Selegård, A. Klasson, F. Söderlind, N. Abrikossova, C. Skoglund, T. Bengtsson, M. Engström, P.-O. Käll, K. Uvdal, *Langmuir* 2010, 26, 5753.
- [48] J. S. Ananta, B. Godin, R. Sethi, L. Moriggi, X. Liu, R. E. Serda, R. Krishnamurthy, R. Muthupillai, R. D. Bolskar, L. Helm, M. Ferrari, L. J. Wilson, P. Decuzzi, Nat. Nanotechnol. 2010, 5, 815.
- [49] T. Courant, V. G. Roullin, C. Cadiou, M. Callewaert, M. C. Andry, C. Portefaix, C. Hoeffel, M. C. de Goltstein, M. Port, S. Laurent, L. V. Elst, R. Muller, M. Molinari, F. Chuburu, Angew. Chem., Int. Ed. 2012, 51 9119
- [50] A. Dash, B. Blasiak, B. Tomanek, F. van Veggel, J. Phys. Chem. C 2018, 122, 11557.
- [51] K. Ni, Z. Zhao, Z. Zhang, Z. Zhou, L. Yang, L. Wang, H. Ai, J. Gao, Nanoscale 2016, 8, 3768.
- [52] N. Pothayee, S. Balasubramaniam, N. Pothayee, N. Jain, N. Hu, Y. Lin, R. M. Davis, N. Sriranganathan, A. P. Koretsky, J. S. Riffle, J. Mater. Chem. B 2013, 1, 1142.
- [53] M. W. Rotz, K. S. Culver, G. Parigi, K. W. MacRenaris, C. Luchinat, T. W. Odom, T. J. Meade, ACS Nano 2015, 9, 3385.
- [54] M. Rowe, D. Thamm, S. Kraft, S. Boyes, Biomacromolecules 2009, 10, 983.
- [55] N. Wartenberg, P. Fries, O. Raccurt, A. Guillermo, D. Imbert, M. Mazzanti, Chem. Eur. J. 2013, 19, 6980.
- [56] Z. Zhou, C. Wu, H. Liu, X. Zhu, Z. Zhao, L. Wang, Y. Xu, H. Ai, J. Gao, ACS Nano 2015, 9, 3012.
- [57] Z. Zhou, X. Zhu, D. Wu, Q. Chen, D. Huang, C. Sun, J. Xin, K. Ni, J. Gao, Chem. Mater. 2015, 27, 3505.
- [58] T. Asanuma, M. Ono, K. Kubota, A. Hirose, Y. Hayashi, T. Saibara, O. Inanami, Y. Ogawa, H. Enzan, S. Onishi, M. Kuwabara, J. A. Oben, Gut 2010, 59, 258.
- [59] A. Ba-Ssalamah, N. Bastati, A. Wibmer, R. Fragner, J. C. Hodge, M. Trauner, C. J. Herold, M. R. Bashir, B. E. Van Beers, J. Magn. Reson. Imaging 2017, 45, 646.
- [60] H. Cheong, S. S. Lee, J. S. Lee, J. Kim, S. W. Kim, W. J. Lee, J. Magn. Reson. Imaging 2015, 41, 1218.
- [61] A. F. Costa, A. T. St-Germain, M. Abdolell, R. L. Smoot, S. Cleary, K. S. Jhaveri, J. Comput. Assisted Tomogr. 2018, 42, 380.



www.advhealthmat.de



- [62] Y. Ding, S. X. Rao, T. Meng, C. Z. Chen, R. C. Li, M. S. Zeng, Eur. Radiol. 2014, 24, 959.
- [63] K. Kubota, T. Tamura, N. Aoyama, M. Nogami, N. Hamada, A. Nishioka, Y. Ogawa, Oncol. Lett. 2012, 3, 990.
- [64] S. S. Lee, S. H. Park, World J. Gastroenterol. 2014, 20, 7392.
- [65] T. Tonan, K. Fujimoto, A. Qayyum, Y. Morita, O. Nakashima, N. Ono, A. Kawahara, M. Kage, N. Hayabuchi, T. Ueno, J. Gastroenterol. Hepatol. 2012, 27, 789.
- [66] S. Chitturi, G. C. Farrell, Semin. Liver Dis 2001, 21, 027.
- [67] H. K. Seitz, F. Stickel, Biol. Chem. 2006, 387, 349.
- [68] Y. C. Cao, J. Am. Chem. Soc. 2004, 126, 7456.
- [69] E. Jung, T. Yu, W. S. Kim, Korean J. Chem. Eng. 2016, 33, 683.
- [70] S. Seo, H. Yang, P. H. Holloway, J. Colloid Interface Sci. 2009, 331, 236.
- [71] R. Si, Y. W. Zhang, H. P. Zhou, L. D. Sun, C. H. Yan, Chem. Mater. 2007, 19, 18.
- [72] G. Singh, B. H. McDonagh, S. Hak, D. Peddis, S. Bandopadhyay, I. Sandvig, A. Sandvig, W. R. Glomm, J. Mater. Chem. B 2017, 5, 418.
- [73] J. Q. Yuan, E. W. Peng, J. M. Xuea, J. Mater. Res. 2014, 29, 1626.
- [74] Z. J. Zhou, R. Hu, L. R. Wang, C. J. Sun, G. Fu, J. H. Gao, Nanoscale 2016, 8, 17887.
- [75] T. Paik, T. R. Gordon, A. M. Prantner, H. Yun, C. B. Murray, ACS Nano 2013, 7, 2850.
- [76] G. Z. Liu, C. E. Conn, C. J. Drummond, J. Phys. Chem. B 2009, 113, 15949.
- [77] R. Si, Y. W. Zhang, L. P. You, C. H. Yan, Angew. Chem., Int. Ed. 2005, 44, 3256.
- [78] X. G. Peng, J. Wickham, A. P. Alivisatos, J. Am. Chem. Soc. 1998, 120,
- [79] I. P. Machado, V. C. Teixeira, C. C. S. Pedroso, H. F. Brito, L. C. V. Rodrigues, J. Alloys Compd. 2019, 777, 638.
- [80] W. W. Yu, E. Chang, J. C. Falkner, J. Y. Zhang, A. M. Al-Somali, C. M. Sayes, J. Johns, R. Drezek, V. L. Colvin, J. Am. Chem. Soc. 2007, 129, 2871
- [81] J.-L. Bridot, A.-C. Faure, S. Laurent, C. Rivière, C. Billotey, B. Hiba, M. Janier, V. Josserand, J.-L., V. Coll, L. Elst, R. Muller, S. Roux, P. Perriat, O. Tillement, J. Am. Chem. Soc. 2007, 129, 5076.
- [82] G. A. El-Mahdy, A. M. Atta, H. A. Al-Lohedan, Molecules 2014, 19, 1713
- [83] Y. H. Gad, Radiat. Phys. Chem. 2008, 77, 1101.
- [84] S. Cavus, J. Polym. Sci., Part B: Polym. Phys. 2010, 48, 2497.
- [85] X. Zhang, Q. Zhang, T. Ma, Q. Liu, S. Wu, K. Hua, C. Zhang, M. Chen, Y. Cui, Nanoscale Res. Lett. 2017, 12, 547.
- [86] X. H. Ma, A. Gong, L. C. Xiang, T. X. Chen, Y. X. Gao, X. J. Liang, Z. Y. Shen, A. G. Wu, J. Mater. Chem. B 2013, 1, 3419.
- [87] J. Pencer, F. R. Hallett, Langmuir 2003, 19, 7488.
- [88] K. D. Sattler, Handbook of Nanophysics: Nanomedicine and Nanorobotics, CRC Press, Boca Raton, FL 2010.
- [89] T. Tang, A. Y. Louie, E. M. Gale, P. Caravan, C. T. Farrar, B. Keil, in Contrast Agents for MRI: Experimental Methods (Eds: V. C. Pierre, M. J. Allen) Royal Society of Chemistry, London 2018, p. 499, Ch. 7.
- [90] N. Hoshyar, S. Gray, H. B. Han, G. Bao, Nanomedicine 2016, 11, 673.
- [91] E. Frohlich, Int. J. Nanomed. 2012, 7, 5577.
- [92] S. Aime, P. Caravan, J. Magn. Reson. Imaging 2009, 30, 1259.
- [93] J. Bourquin, A. Milosevic, D. Hauser, R. Lehner, F. Blank, A. Petri-Fink, B. Rothen-Rutishauser, Adv. Mater. 2018, 30, 1704307.
- [94] M. A. Malfatti, H. A. Palko, E. A. Kuhn, K. W. Turteltaub, Nano Lett. 2012, 12, 5532.
- [95] Y. Dai, C. Wu, S. Wang, Q. Li, M. Zhang, J. Li, K. Xu, Nanomedicine 2018, 14, 547.
- [96] X. Tian, F. Yang, C. Yang, Y. Peng, D. Chen, J. Zhu, F. He, L. Li, X. Chen, Int. J. Nanomed. 2014, 9, 4043.

- [97] B. B. Zhang, W. T. Yang, J. N. Yu, W. S. Guo, J. Wang, S. Y. Liu, Y. Xiao, D. L. Shi, Adv. Healthcare Mater. 2017, 6, 11.
- [98] E. J. Ngen, D. Artemov, Int. J. Mol. Sci. 2017, 18, 198.
- [99] L. R. Hirsch, R. J. Stafford, J. A. Bankson, S. R. Sershen, B. Rivera, R. E. Price, J. D. Hazle, N. J. Halas, J. L. West, *Proc. Natl. Acad. Sci.* USA 2003, 100, 13549.
- [100] C. Loo, A. Lin, L. Hirsch, M. H. Lee, J. Barton, N. Halas, J. West, R. Drezek, Technol. Cancer Res. Treat. 2004, 3, 33.
- [101] C. M. Sayes, J. D. Fortner, W. Guo, D. Lyon, A. M. Boyd, K. D. Ausman, Y. J. Tao, B. Sitharaman, L. J. Wilson, J. B. Hughes, J. L. West, V. L. Colvin, *Nano Lett.* 2004, 4, 1881.
- [102] G. J. Todaro, G. K. Lazar, H. Green, J. Cell. Physiol. 1965, 66, 325.
- [103] C.-C. Liang, A. Y. Park, J.-L. Guan, Nat. Protoc. 2007, 2, 329.
- [104] V. S. Perera, G. Chen, Q. Cai, S. D. Huang, Analyst 2016, 141, 2016.
- [105] R. A. Yokel, M. L. Hancock, E. A. Grulke, J. M. Unrine, A. K. Dozier, U. M. Graham, *Nanotoxicology* 2019, 13, 455.
- [106] P. Angulo, N. Engl. J. Med. 2002, 346, 1221.
- [107] E. Bugianesi, N. Leone, E. Vanni, G. Marchesini, F. Brunello, P. Carucci, A. Musso, P. De Paolis, L. Capussotti, M. Salizzoni, M. Rizzetto, Gastroenterology 2002, 123, 134.
- [108] O. James, C. Day, Lancet 1999, 353, 1634.
- [109] G. Vernon, A. Baranova, Z. M. Younossi, *Aliment. Pharmacol. Ther.* 2011, 34, 274.
- [110] N. Chalasani, Z. Younossi, J. E. Lavine, A. M. Diehl, E. M. Brunt, K. Cusi, M. Charlton, A. J. Sanyal, Am. J. Gastroenterol. 2012, 107, 1598.
- [111] N. Fretellier, M. Salhi, J. Schroeder, H. Siegmund, T. Chevalier, P. Bruneval, G. Jestin-Mayer, F. Delaloge, C. Factor, J. F. Mayer, J. M. Fabicki, C. Robic, B. Bonnemain, J. M. Idée, C. Corot, Eur. J. Pharm. Sci. 2015, 72, 46.
- [112] J. Garcia, S. Z. Liu, A. Y. Louie, Philos. Trans. R. Soc., A 2017, 375, 20170180.
- [113] T. Mercantepe, L. Tümkaya, F. B. Çeliker, Z. Topal Suzan, S. Çinar, K. Akyildiz, F. Mercantepe, A. Yilmaz, J. Magn. Reson. Imaging 2018, 48. 1367.
- [114] G. Marchesini, M. Brizi, G. Bianchi, S. Tomassetti, E. Bugianesi, M. Lenzi, A. J. McCullough, S. Natale, G. Forlani, N. Melchionda, *Diabetes* 2001, 50, 1844.
- [115] J. P. Lerch, L. Gazdzinski, J. Germann, J. G. Sled, R. M. Henkelman, B. J. Nieman, Front. Neuroinf. 2012, 6, 6.
- [116] C. Tempel-Brami, Y. S. Schiffenbauer, A. Nyska, N. Ezov, I. Spector, R. Abramovitch, R. R. Maronpot, *Toxicol. Pathol.* 2015, 43, 633.
- [117] L. J. Dixon, M. Barnes, H. Tang, M. T. Pritchard, L. E. Nagy, Compr. Physiol. 2013, 3, 785.
- [118] X. Y. Feng, T. T. Deng, Y. Zhang, S. B. Su, C. J. Wei, D. S. Han, Immunology 2011, 132, 287.
- [119] D. Frausto-Del-Rio, I. Soto-Cruz, C. Garay-Canales, X. Ambriz, G. Soldevila, J. Carretero-Ortega, J. Vazquez-Prado, E. Ortega, Cytokine 2012, 57, 158.
- [120] K. Kazankov, S. M. D. Jorgensen, K. L. Thomsen, H. J. Moller, H. Vilstrup, J. George, D. Schuppan, H. Gronbaek, Nat. Rev. Gastroenterol. Hepatol. 2019, 16, 145.
- [121] T. A. Kerr, N. O. Davidson, Hepatology 2012, 56, 1995.
- [122] S. Thuy, R. Ladurner, V. Volynets, S. Wagner, S. Strahl, A. Konigsrainer, K. P. Maier, S. C. Bischoff, I. Bergheim, J. Nutr. 2008, 138, 1452.
- [123] A. Varin, S. Mukhopadhyay, G. Herbein, S. Gordon, *Blood* 2010, 115, 353.
- [124] L. Pasquini, A. Napolitano, E. Visconti, D. Longo, A. Romano, P. Toma, M. C. R. Espagnet, CNS Drugs 2018, 32, 229.
- [125] G. D. Christian, Anal. Chem., 6th ed., John Wiley and Sons Inc., Hoboken, NJ 2003, p. 111.